

THE MASSES OF SUPERNOVA REMNANT PROGENITORS IN M83

BENJAMIN F. WILLIAMS,¹ TRISTAN J. HILLIS,¹ WILLIAM P. BLAIR,² KNOX S. LONG,^{3,4} JEREMIAH W. MURPHY,⁵
ANDREW DOLPHIN,⁶ RUBAB KHAN,¹ AND JULIANNE J. DALCANTON¹

¹*Department of Astronomy, Box 351580, University of Washington, Seattle, WA 98195; ben@astro.washington.edu; tjhillis@uw.edu; rubab@uw.edu; jd@astro.washington.edu*

²*Department of Physics and Astronomy, Johns Hopkins University, 3400 North Charles Street, Baltimore, MD 21218; wblair@jhu.edu*

³*Space Telescope Science Institute, 3700 San Martin Drive, Baltimore MD 21218, USA; long@stsci.edu*

⁴*Eureka Scientific, Inc. 2452 Delmer Street, Suite 100, Oakland, CA 94602-3017*

⁵*Department of Physics, Florida State University, jwmurphy@fsu.edu*

⁶*Raytheon, 1151 E. Hermans Road, Tucson, AZ 85706; adolphin@raytheon.com*

ABSTRACT

We determine the ages of the young, resolved stellar populations at the locations of 237 optically-identified supernova remnants in M83. These age distributions put constraints on the progenitor masses of the supernovae that produced 199 of the remnants. The other 38 show no evidence for having a young progenitor and are therefore good Type Ia SNR candidates. Starting from Hubble Space Telescope broadband imaging, we measured resolved stellar photometry of seven archival WFC3/UVIS fields in F336W, F438W, and F814W. We generate color-magnitude diagrams of the stars within 50 pc of each SNR and fit them with stellar evolution models to obtain the population ages. From these ages we infer the progenitor mass that corresponds to the lifetime of the most prominent age that is <50 Myr. In this sample, there are 47 SNRs with best-fit progenitor masses $>15 M_{\odot}$, and 5 of these are $>15 M_{\odot}$ at 84% confidence. This is the largest collection of high-mass progenitors to date, including our highest-mass progenitor inference found so far, with a constraint of <8 Myr. Overall, the distribution of progenitor masses has a power-law index of $-3.0^{+0.2}_{-0.7}$, steeper than Salpeter initial mass function (-2.35). It remains unclear whether the reason for the low number of high-mass progenitors is due to the difficulty of finding and measuring such objects or because only a fraction of very massive stars produce supernovae.

Keywords: Stellar Evolution — Massive Stars — Supernovae

1. INTRODUCTION

One of the most fundamental predictions from stellar evolution theory is that stars above a certain mass end their lives in powerful supernova (SN) explosions. SNe play major roles in exciting and enriching the interstellar medium, as well as in regulating star formation and creating compact objects that can become significant emitters of X-rays, Gamma-rays, and even gravitational waves.

Nearby SNe are well-observed and cataloged (e.g., Guillochon et al. 2017). However, they are limited in number and the masses of the progenitor stars are often very difficult to discern. Traditionally, direct imaging of progenitors has been the method of choice for constraining core-collapse supernovae (CCSNe) progenitor masses, but it has substantial limitations. High-quality precursor imaging must exist, and the astrometry must be sufficiently accurate ($\sim 0.1''$) to identify the exact star that exploded. Furthermore, even when the progenitor is identified, interpretation of its photometry depends on the most uncertain stages of stellar evolution (Gallart et al. 2005). The mass of a precursor is typically estimated by fitting stellar evolution models to the star’s color and magnitude (e.g. Chen et al. 2015); however, mass loss, binary evolution, pulsation, internal mixing, and the formation of dust in stellar winds all contribute to systematic and random uncertainties in late-stage evolutionary models. Therefore, matching a stellar evolution model to a single evolved star places uncertain constraints on the initial mass.

To date, archives of extragalactic resolved stellar imaging from the *Hubble Space Telescope* (*HST*) have yielded 68 direct-image constraints; of these, only 30 are detections, and the rest are upper limits (e.g., Smartt 2015; Van Dyk 2017, for recent reviews). While the statistics from the direct-imaging technique are low, they already lead to some interesting conclusions and hints. For example, *HST* archival data shows that the most common supernovae (SNe), Type II-P, map to red supergiant progenitors (Smartt 2009). Smartt (2015) present 18 detections and 27 upper limits and infer a minimum mass of $7_{-1}^{+4} M_{\odot}$ for SN IIP. They also infer an upper mass for SN IIP of $\sim 17 M_{\odot}$. Yet, red supergiant masses are estimated up to $\sim 25 M_{\odot}$. As a result, they conclude that the most massive red supergiant progenitors may not explode as SNe. More recently, Davies & Beasor (2017) suggest that the bolometric corrections for red supergiants that are about to explode are much larger than were used in the Smartt (2015) analysis. Using bolometric corrections calibrated with very evolved red supergiants, Davies & Beasor (2017) infer a maximum mass of $27 M_{\odot}$, suggesting that even the most massive red supergiants may indeed explode. There are very few potential direct-imaging progenitor estimates for

type Ib or Ic SNe, which have been difficult to interpret but may suggest high mass progenitors (e.g., Cao et al. 2013; Groh et al. 2013; Bersten et al. 2014; Fremling et al. 2016; Eldridge & Maund 2016; Van Dyk et al. 2018; Kilpatrick et al. 2018; Xiang et al. 2019). Because of the small sample of direct-imaging measurements, the mapping between progenitors and SN type remains unclear (e.g. Smartt et al. 2009; Anderson et al. 2012; Smartt 2015; Adams et al. 2017a; Davies & Beasor 2017).

There are a few methods of indirectly constraining progenitor masses (e.g., Anderson et al. 2012). The technique we apply in this paper is age-dating of the surrounding stellar population of a SNR. This method relies on the fact that only relatively massive stars ($>7.5 M_{\odot}$) become CCSNe (Jennings et al. 2012; Díaz-Rodríguez et al. 2018). Thus, their lifetimes are limited to <50 Myr (Girardi et al. 2002). Over 90% of stars form in clusters containing more than 100 members with $M_{\text{cluster}} > 50 M_{\odot}$ (Lada & Lada 2003). These stars remain spatially correlated on physical scales up to ~ 100 pc during the 100 Myr lifetimes of $4 M_{\odot}$ stars, even if the cluster is not gravitationally bound (Bastian & Goodwin 2006). We have confirmed this expectation empirically in several cases (Badenes et al. 2009; Gogarten et al. 2009; Murphy et al. 2011; Williams et al. 2018). Thus, it is reasonable to assume a physical association between any observed CCSN and other young stars of the same age and in the same vicinity. We use the median star formation age, going to 50 Myr ($7.3 M_{\odot}$ precursor equivalent, see Section 2.7 for details), to infer a progenitor mass using our chosen models. Therefore, once the surrounding population age is constrained, one may infer the precursor mass through stellar evolution models without the need for precursor imaging (see Jennings et al. 2012; Jennings et al. 2014 hereafter J14; Williams et al. 2014a, for more details on the technique).

Using this population age-dating method, one may estimate a progenitor mass for any location within 8 Mpc where there has been a CCSN. To date, there are only 39 observed SNe within this volume (Guillochon et al. 2017); however, there are thousands of supernova remnants (SNRs) in this volume. These SNRs mark the locations of SNe for ~ 20 kyr or more (Braun et al. 1989), and if they reside in regions with recent star formation, they are likely to be from CCSNe. Thus, if we use SNRs for measuring progenitor masses, we improve our time baseline for finding CCSNe locations by a factor of more than 200.

Studies of precursor masses of SNRs have yielded promising results on constraining the distribution of stellar masses that produce supernovae. J14 constrained progenitor masses for 115 SNRs in M31 and M33, finding that their mass distribution was steeper than a standard Salpeter initial mass function (IMF), and detecting a clear lower mass limit to their distribution at $\sim 7.5 M_{\odot}$. Díaz-Rodríguez et al.

(2018) updated and re-examined 94 of those SNRs using a more uniform photometric sample and a Bayesian treatment of contamination and uncertainties. They confirm the J14 results, and place reliable uncertainties on both the power-law index of the mass distribution ($-3.0^{+0.5}_{-0.3}$) and the lower mass cutoff ($7.33^{+0.02}_{-0.16}$).

Herein, we seek to extend these studies to the nearby galaxy M83. M83 is a strong candidate for this kind of study because of its proximity (4.61 Mpc; Saha et al. 2006), a nearly face-on view at ($i=24^\circ$; Lundgren et al. 2004), and its long history of SNe (Richter & Rosa 1984). As searches for SNRs within M83 (Blair & Long 2004; Dopita et al. 2010; Blair et al. 2012, 2014) have shown, this galaxy is rich with past supernova activity, with 307 SNRs and SNR candidates, which is more than the combined M31+M33 sample of J14. This gives us improved statistical power, for the progenitor masses of SNe. With such a large sample we can place improved constraints on the distribution of progenitor masses and on the upper mass limit for CCSNe progenitors.

In this paper, Section 2 discusses the archival *HST* data, and the analysis technique we use for estimating progenitor masses. Section 3 details our resulting progenitor age and mass estimates. Section 4 investigates the distribution of progenitor masses in the context of standard mass functions, and we conclude with a brief summary in Section 5. We assume a distance of 4.61 Mpc (Saha et al. 2006) throughout the paper, and we use the Padova (Girardi et al. 2002; Marigo et al. 2008; Girardi et al. 2010) stellar evolution model library for all of the model fitting and for all stellar lifetime estimates.

2. DATA & ANALYSIS

We analyze *HST* observations of seven WFC3/UVIS fields in three filters F336W, F438W, and F814W covering most of the high surface brightness portion of M83. These observations are described in detail in Blair et al. (2014). In the subsections that follow, we discuss the origin of the SNR positions we analyzed, our technique for measuring resolved stellar photometry, our method for fitting models to the photometry to determine the ages of the stellar populations, and our process for inferring progenitor masses from these ages.

2.1. Supernova Remnant Locations

We took the locations of SNRs and strong SNR candidates in M83 from a compilation of catalogs obtained by several surveys. We provide the full combined catalog in Table 1. The survey where most of the SNRs were discovered was from the Magellan 6.5 m telescope at Las Campanas (Blair et al. 2012, B12 in the Table). Those SNR candidates found first using *HST* are from Dopita et al. (2010) and Blair et al. (2014), which are D10 and B14 in the Table.

We note that the Dopita et al. (2010) catalog covered the complex starburst nucleus where confusion effects prevent resolved photometry even for *HST*, so many of these objects are excluded from the photometric analysis. There are a handful of SNR candidates in both the Magellan data set and the *HST* data that have not been reported previously but are included here for completeness. For the SNRs that have identified X-ray counterparts from Long et al. (2014, L14 in the Table), a cross reference is also provided. Spectroscopic confirmations of a significant subsample of these SNRs were reported by Winkler et al. (2017). Furthermore, there are six historical SNe whose locations are well-determined, which we also include in the sample. An additional young SNR that may represent an unobserved SN in the last century, SNR 238 (B12-174a), is also included (Blair et al. 2015). Table 1 represents the most complete listing of SNRs and good SNR candidates in M83 to date.

Table 1 also includes a quality flag for each SNR candidate, based on the amount of supporting evidence used to confirm the object is a SNR. The quality flag values indicate the following categories:

- 1a: Optical imaging candidate confirmed by spectroscopy and having X-ray emission.
- 1b: Optical imaging candidate strongly confirmed by optical spectroscopy (e.g. spectroscopic [S II]:H α > 0.5) but no X-ray detection.
- 1c: Optical imaging candidate with photometric [S II]:H α > 0.5 but no optical spectral confirmation available and no X-ray detection.
- 1d: Optical imaging candidate with X-ray but no spectra available.
- 1e: Optical imaging candidate with X-ray but marginal spectral ratio (likely due to H II contamination).
- 1f: Solid Imaging candidate, no X-ray, but with clear H II contamination in spectrum.
- 1g: Strong *HST* [Fe II] 1.64 μ m candidate
- 1h: *HST* Nuclear candidates (mostly Dopita et al. 2010) with no additional supporting evidence.
- 1z: Special cases.
- 2: Optical candidate with imaging or spectroscopic ratio $0.25 < [S II]:H\alpha < 0.5$. Many of these are likely SNRs, but H II contamination causes uncertainty. Some have detectable [Fe II], which strengthens their case.
- h: Historical supernova (event was observed).

Finally, the catalog has a use flag column, which indicates how each SNR was used or not used in the analysis. This flag as the following categories:

- p: Progenitor mass constrained from measured local young population.

- n: No young population detected in the fit (Type Ia candidate).
- o: Outside of the HST coverage; no measurement performed.
- c: Too close to the center of M83; no measurement performed.
- i: Insufficient photometry for a measurement; fitting failed.

In Figure 1, we show the locations of all of the SNRs for which we were able to obtain sufficient photometry for a measurement (use flags “p” and “n”). The circles mark remnants of use flag “p” and are color-coded by the most likely progenitor mass from our technique. Yellow squares mark the locations of remnants with “n” use flags.

The SNR catalog has 307 historical SNe, SNRs, and SNR candidates. There are 271 of these within the 7-field HST/UVIS footprint for which we have resolved stellar photometry. However, 24 of those locations are too close to the complex galaxy nucleus to provide reliable resolved stellar photometry. Of the remaining 247 SNRs, 10 more had samples that proved insufficient to allow the fitting to converge. Our final measured sample therefore consisted of 237 SNR locations (see Figure 1) and a 100 random control sample positions.

For our program, we first ran photometry on all of the resolved stars in the HST imaging data. Then, to quantify the errors and completeness of the photometry as a function of star color, magnitude, and location, we ran over a million artificial star tests. As in previous population-based progenitor studies, we then fit the photometry data within 50 pc of each SNR with stellar evolution models to constrain the age distribution of the young stars near each SNR. We now discuss the production and analysis of our resolved stellar photometry.

2.2. Photometry

We measured resolved stellar photometry from the F336W, F438W, and F814W imaging with the point spread function (PSF) fitting photometry pipeline used for the Panchromatic Hubble Andromeda Treasury (PHAT; Williams et al. 2014b). In short, this pipeline uses an astrodizzle PyRAF routine to flag cosmic-ray affected pixels, and the DOLPHOT (Dolphin 2000, 2016) PSF-fitting photometry package with the TinyTim-generated PSFs (Krist et al. 2011a) to find and measure point source photometry for all sources in a set of HST images. It starts by reading all of the `flc` images into memory to search for stars using the full image stack. Then the photometry is performed on the individual `flc` images, where a PSF is

fitted to the location of all star locations in every image. For the multiple exposures in a given filter, the measurements are combined to reduce the photometric uncertainty and increase the signal to noise of the measurements.

The pipeline has been updated based on some of the detailed tests performed on the PHAT photometry. In particular, we used the TinyTim PSFs (Krist et al. 2011b) and we used the CTE-corrected `flc` images for photometry instead of post-photometry CTE corrections. Both of these updates have resulted in more precise photometry with smaller systematic uncertainties.

From the DOLPHOT measurements, we first produced full-field color-magnitude diagrams (CMDs) of our photometry. We show examples of these in Figure 2, where it is clear that we have detected the upper main-sequence of blue stars. At the distance of M83, the depth of these CMDs is to $m_{F435W} \sim 26$; $M_{F435W} \sim -2.5$, which corresponds to a main-sequence turnoff age of 70 Myr, which is the lifetime of a $6.3 M_{\odot}$ star in the Padova models. Therefore we are sensitive to all populations relevant for CCSNe progenitor measurements.

After this check, we focused our further analysis on the regions within 50 pc of each SNR location, and on a control set of photometry taken from random positions of the same physical size. These control regions were distributed in proportion to the real SNRs in each of the 7 M83 UVIS fields, and their photometry samples were run through the same analysis routines as those of the SNR regions. The results from the control samples allow us to quantitatively check that the measurements from the SNR locations differ from the field. Examples of the relevant regions around several SNRs are shown in Figure 3 to demonstrate how well-resolved the individual stars are and to show the diversity of the dust and stellar density properties of the regions.

2.3. Artificial Star Tests

Fitting CMDs with models requires convolving models with the errors, bias, and completeness of the photometry at each color and magnitude. These quantities are best determined through artificial star tests (ASTs), whereby a star of known location, color, and brightness is added to the images, and then the photometry of that section of the images is rerun. This operation is run hundreds of thousands to millions of times to cover location, color, and brightness space well enough to properly model the photometric quality of each CMD that we fit.

We ran ASTs covering the range of colors and magnitudes seen in the observed stellar catalogs. The differences between the input star properties and the output measurements allow us to calculate the bias, uncertainty, and completeness of the observed stellar catalog as a function of star color, and magnitude, and environment. These quality metrics are

then used by the fitting software to convolve model CMDs so that they have the same photometric quality as the observed CMDs. Then we can determine the model CMD that best matches the observed CMD.

ASTs require significant computational resources as they require running the photometric measurements many times. Therefore, to increase the efficiency of ours, we assume regions of similar stellar density and exposure time will have resolved star samples of the same photometric quality. This assumption allows us to apply one set of ASTs to several SNRs. A similar technique was used by the PHAT team to drastically decrease the number of ASTs necessary to measure SFHs as a function of position over the large area covered by the PHAT project (Williams et al. 2017).

To optimize the efficiency of our ASTs, we first measured the relative stellar density as a function of position in the images. To avoid biases due to completeness differences we limited the magnitude range over which we counted stars to where the completeness was high ($>80\%$) over the entire survey ($F438W < 26.2$). At each image location, we counted stars above this brightness limit within 50 pc and divided by the area to determine the stellar density.

We then tested the assumption that ASTs taken from regions of similar stellar density are interchangeable. For this test, we ran ASTs at the location of an observed stellar sample, as well as in another location in the image with similar stellar density. We then fit the observed CMD of one of the locations twice: once with each set of AST results. We found that ASTs from locations with stellar densities within a factor of two of one another resulted in equivalent age measurements. Thus, we performed 42 sets of ASTs obtained from regions spanning the full range of stellar densities in our sample (0.4 to 20 arcsec $^{-2}$), and stay well within this factor of two variation. We then applied this library of ASTs during model fitting to our photometry. Namely, when fitting each SNR and control sample, we convolved the models with the photometric errors, bias, and completeness by applying the ASTs measured from a region of appropriate stellar density.

2.4. Deriving Star Formation Histories

We employ the CMD fitting package MATCH (Dolphin 2002, 2013), which fits the CMDs from resolved stellar photometry to determine the best star formation history (SFH) of each stellar sample near a SNR and control region. The SFH is the distribution of stellar ages and metallicities present in the sample, as well as the uncertainties on that distribution. This package has been used by many investigators to measure the star formation rate as a function of lookback time for a number nearby galaxies (e.g., Williams et al. 2009; McQuinn et al. 2010; Weisz et al. 2011; Skillman et al. 2017, and many others), as well as

to measure star cluster ages (e.g., Senchyna et al. 2015), and the ages and masses of supernova progenitors (e.g., Murphy et al. 2011; Jennings et al. 2012, J14).

We applied time bins starting at 6.6 to 8.0 log years in steps of 0.05 dex and then from 8.0 to 10.1 log years in steps of 0.1 dex using Padova isochrones (Girardi et al. 2002; Marigo et al. 2008; Girardi et al. 2010). Furthermore, we constrain the present day metallicity from $-0.6 \leq [Fe/H] \leq 0.1$, as appropriate for M83 (Bresolin et al. 2009). We also applied reddening (A_V) and differential reddening (dA_V) to our model fits (see Section 2.5). In addition, the MATCH package allows the inclusion of a contamination CMD to look for populations that are present in the sampled region at higher density than the surrounding field. We used the entire WFC3 $162'' \times 162''$ UVIS M83 field surrounding the SNR, scaled to the area of the extraction region area, for this contamination CMD.

2.5. Determining foreground and differential extinction

M83 is characterized by an abundance of dust embedded in the disk. For extinction, it is valuable to consider multiple colors. Therefore, we consider both the F336W-F438W and F438W-F814W CMDs when finding the extinction properties of each location. These extinction properties are both the overall extinction affecting the entire location, A_V (with the minimum bounded by the foreground Galactic extinction of 0.2; Schlafly & Finkbeiner 2011), and extinction spread due to the distribution of stars along the line of sight (dA_V). Each of these parameters affect the CMD differently, and are therefore they are applied to the models independently. First, A_V is applied to all of the stars in each model CMD. Then dA_V is applied to the model CMD to spread the stars along the reddening line as they would be if they were randomly distributed within a uniform dust layer. In essence, A_V affects the location of features in the CMD (e.g., the main sequence), while dA_V affects the sharpness of the features in the CMD. For example, stars embedded within dusty regions of a galaxy (high dA_V) will produce CMDs with features smeared along the reddening line, even if they are behind little foreground A_V , while stars not embedded in a dusty region (low dA_V) will produce CMDs with sharp features, even if all of the stars behind a large foreground A_V .

We determine the values for A_V and dA_V by finding the best maximum-likelihood fit value reported by MATCH (Dolphin 2012) for a grid of possibilities when fitting (see Figures 4 and 5). We then fix the A_V and dA_V values to those determined from the multiple colors when fitting the deepest single CMD for the final age distribution and uncertainties out of these, as described below.

2.6. Uncertainties

Our uncertainties are mainly due to photometric error, incompleteness, and the number of stars in our sample available to constrain the age distribution of the young component of the population. All of these vary significantly for the SNR sample. For example, the number of stars ranges from 10s to 100s of stars per SNR. Thus we measure the uncertainties separately for each SNR sample.

We characterize these uncertainties using a hybrid Monte-Carlo (MC) algorithm within MATCH using the task `hybridMC` (Dolphin 2013). This task accepts or rejects thousands of potential SFHs surrounding the best fitting one, based on likelihood. It then applies the distribution of accepted SFHs to determine the 68% uncertainty regions surrounding the best fit. The `hybridMC` uncertainty determination applies statistics that are valid only for independent CMDs. Applying these statistics to 2 CMDs that share a filter would produce incorrect uncertainties because the CMDs are correlated. Therefore, we must choose one of our CMDs when fitting for the final SFHs and uncertainties. The M83 data contain imaging in F336W, F438W, and F814W.

To determine which CMD fit to use for our final SFH and uncertainties, we fit both the F336W vs. F336W-F438W and the F438W vs. F438W-F814W CMD independently, fixing A_V and dA_V measured values (see Section 2.5). We then compared the best-fit SFH to the best-fit SFH from the simultaneous fit of both CMDs. We found overall consistency between the techniques, but the single CMD fits had reliable uncertainties. The best constraints were almost always from the fits to the F336W vs. F336W-F438W CMDs. This result was expected because the F814W photometry is the shallowest and least sensitive to the young populations. However, there were a handful of cases, mostly those with the highest reddening, where the F336W-F438W CMD alone did not produce a result consistent with the 2 CMD fit from the A_V , dA_V runs (185, 278, 059, 197, 090, 117, 150, 227, 246, SN1950B). In these cases we found that the fit to the F438W vs. F438W-F814W CMD produced a result consistent with the 2 CMD fit. We report as our final measurement of the SFH and uncertainties, the results from the F336W vs. F336W-F438W CMD, except for these exceptions.

2.7. Progenitor Mass

Our method for constraining the progenitor mass is similar to that of previous work (e.g., Jennings et al. 2012; J14; Williams et al. 2018). The method begins by finding the most likely age of the progenitor star. In short, we measure the SFH from broadband photometry of the resolved stars within 50 pc of the location of each SNR. This region size assumes that most young stars are coeval within our desired extracted region, as suggested by the

work of (Bastian & Goodwin 2006). Indeed, the validity of this assumption has been strengthened by the works of Gogarten et al. (2009) and Murphy et al. (2011).

We restrict the ages in the SFH that we apply to our progenitor analysis. The ages of SNR progenitors measured with deeper photometry in more nearby galaxies have established that the maximum progenitor age for CCSNe is <50 Myr (young enough for a $\sim 7 M_{\odot}$ star to still exist). While older progenitors are allowed according to binary evolution models (Xiao et al. 2019, e.g.,), a maximum of 50 Myrs is empirically measured for CCSNe progenitors by J14 and confirmed by Díaz-Rodríguez et al. (2018) in M31 and M33, even when they include older ages in their analysis. Furthermore Xiao et al. (2019) find a similar empirical age constraint using an independent emission line fitting technique that uses the latest binary evolution models to infer ages of HII regions that have hosted CCSNe.

We take advantage of these empirical results to limit the part of the SFH that we apply to determine the progenitor mass. We assume only the part of the SFH <50 Myr is relevant for determining progenitor ages. When we infer the most likely progenitor age of each SNR, we look for the most prominent peak in the age distribution, only considering ages <50 Myr. This assumption means that we are not able to use these data to probe the high-age (low-mass) end of the progenitor mass function, but it allows us to avoid including the higher age bins, which have large uncertainties at the photometric depth of the observations used here, into our age determinations.

We derive the mass fraction for each time bin over the past 50 Myrs, taking advantage of the empirical constraints so that we do not need to include older ages that have main sequence turnoffs near our completeness limit which lead to large SFH uncertainties. Furthermore, these older bins are more likely to contain stars unrelated to the SNR progenitor because stars of older ages have had more time to migrate away from their siblings. Thus, limiting the ages to those known to be relevant to CCSNe progenitors helps to minimize contamination from unrelated populations.

Figures 4 and 5 summarize the progenitor mass measurement technique for two SNR locations (SNR 295 and SNR 057, respectively). We include figures of this format for all 199 SNRs with progenitor constraints in the supplemental materials. The effect of the assumed differential extinction is shown in the upper-left panel, where the resulting age distribution from each assumed differential extinction amount is plotted with a different color. In Figure 4 the general pattern in ages is relatively insensitive to the assumed dA_V . The lower-left panels of the figure show the star formation history (SFH) along with uncertainties for the best dA_V result. Peaks in the rate and stellar mass fraction correspond to the most likely progenitor age.

The full SFHs show how well the median age represents the full age distribution of the population. An age distribution may correspond to several epochs of SF or may be dominated by one epoch. In the case of the former, the median age is less likely to represent the correct age of the progenitor. The full probability distribution for each event is a more precise characterization of the complex uncertainties.

Based on these measurements, we use the age where 50% of the stars (as determined from the bottom-center panel) have formed as the most likely progenitor age. We then take our uncertainties to include all ages that may contain the median age. This is shown with the tan vertical shaded region in the bottom left panel of the mass measurement figures (e.g. Figures 4 and 5). These limits define our 1σ progenitor age range for the progenitor mass. From this age range, we infer the zero age main sequence (ZAMS) mass range using the Girardi et al. (2010) isochrone library as a lookup table for the most massive star present at any given age. We set a floor for the uncertainty to be at least $0.1 M_{\odot}$. In the cases where we find there to be zero SF in the last 50 Myrs, we assume these to be the remnants of Type Ia supernovae or runaway massive stars, and we provide no measurement of M_{ZAMS} .

3. RESULTS

After completing our measurements of the recent SFHs surrounding all of the SNRs and converting these to probability distributions, we generated Table 2 describing all SNRs including the masses corresponding to the median ages surrounding each. In column 1 we give the identifier of the SNR. Columns 2 to 4 specify the 50% completeness magnitudes for each SNR for the three filters in our analysis. Note these cutoffs are derived from the 50% completeness of the respective fake star sets; hence, SNRs utilizing the same fake stars will have the same magnitude cutoffs (see § 2.3). Column 5 gives the number of stars extracted from each region in the F438W data. Columns 6 and 7 give the best differential reddening and reddening applied during the fitting process, respectively. Lastly, column 8 gives the inferred M_{ZAMS} from the median age with bounds. When an SNR is missing values in column 8 this means either we were not able to measure the SFH or we found there to be no SF in the past 50 Myrs (see Table 1 use flags n, o, c, and i). Within this table we only include SNRs where we were able to put a constraint on the progenitor mass (use flag "p").

In Table 3 we show the calculated age probability distribution for an SNR as the fraction of stellar mass present in each age bin. The supplemental materials contain similar information for all of the SNRs we measured. In columns 1 and 2 we define the edges of the age bin (T1 and T2) with T1 being the more recent look back time. Column 3 gives the best-fit star formation rate, SFR(best), for that age bin while

columns 4 and 5 are the negative and positive uncertainties on that rate. Column 6, PDF(best), gives the fraction of the <50 Myr stellar mass in that age bin according to the best-fit SFH, and columns 7 and 8 provide the uncertainties on that fraction, given the rate errors in Columns 4 and 5. Column 8, CDF(best), gives the running cumulative fraction of stellar mass as a function of time for the best-fit SFH. Columns 9, 10, and 11 provide the 16th, 50th, and 84th percentiles of the cumulative mass fraction for a set of 10^6 realizations of the SFH with the uncertainties in Columns 4 and 5. Columns 12 and 13 show the masses of stars with lifetimes that match the edges of the age bin (M1 and M2). Table 3 corresponds to Figure 4 which has multiple epochs of SF according to the bottom-middle and bottom-right panels. We see that the progenitor is more likely to belong to the peak at 25 Myr.

4. DISCUSSION

We now investigate the total distribution of masses in our sample as well as looking for spatial correlations between progenitor mass and galactic structure.

4.1. Spatial Distribution As Function of Mass

The derived progenitor masses are plotted on an image of M83 in Figure 1 to show the spatial distribution as a function of derived progenitor mass. The symbol colors denote derived mass with masses above $20 M_{\odot}$ shown as red, and lower mass ranges progressing from orange to green to blue. Yellow squares designate those SNRs for which no young stellar population was identified, and these are the candidates for SNIa progenitors. The higher mass progenitors generally follow the spiral arms, but we note that the most massive progenitor masses appear to be most closely associated with arms and/or star forming regions. This result is consistent with findings in clustering studies that show trends where stars of higher masses are more clustered (e.g., Kang et al. 2009; Bianchi et al. 2012; Kim et al. 2012). Lower mass progenitors, while also associated with the arms and star forming regions, seem to show a broader spatial distribution. We also see that the Type Ia candidates tend to be even more generally distributed, including the interarm regions.

4.2. Progenitor Mass Distribution

Our sample of 199 SNe and SNRs with inferred progenitor masses is the largest ever produced for any single galaxy. Thus the distribution has the potential to yield the tightest constraints on the shape of the progenitor mass distribution to date. We plot the distribution of all the progenitor masses in Figures 6 and 7. Figure 6 shows a histogram of the progenitor mass distribution for M83 along with the combined M31+M33 distribution for comparison. While the number

of progenitors in the lowest mass bin is comparable in Figure 6, the fraction of the total in that lowest bin is less, with significantly more progenitors in the 10 – 15 M_{\odot} range and near 20 M_{\odot} . The M83 distribution has a significantly higher proportion of higher-mass progenitors as well.

In Figure 7, the data points mark the masses at the median ages as described in § 2.6, along with their uncertainties. They are plotted in order of mass to show the cumulative mass distribution. Lines mark fits from various power-law mass distributions. The left panel is the best-fit to the data, with an index of $-3.0^{+0.2}_{-0.7}$ ($\chi^2/dof < 1.1$). The middle panel has lines drawn from a Kroupa IMF (index of 2.3), and the right panel has lines drawn from the index 4.4 that fits the M31+M33 SNR distribution from J14. Note that this plot excludes the assumed Type Ia supernovae, or objects where no young stellar population was detected.

In addition, we can study only the spectroscopically-confirmed SNR sample (quality flag 1a in the Table 1), along with the observed SNe, which comprises a subsample of 40. The mass distribution of this subsample has a best-fitting power-law index of 2.8, making it slightly closer to a standard IMF. Moreover, a more recent re-analysis of the M31+M33 progenitor distribution that uses Bayesian inference to better account for the uncertainties, finds a power-law index for that distribution of $-3.0^{+0.3}_{-0.5}$ (Díaz-Rodríguez et al. 2018), which is consistent with this M83 result.

We also compare the SNR distribution to the control sample. The first difference is that the random positions have double the fraction of locations with no young population. In addition, the distribution of inferred masses for the random positions is significantly steeper, with a best-fit power-law index of -3.7 . The SNR locations appear to be providing a distribution different from the general field. The fact that the random field is steeper and that the spectroscopically-confirmed sample is less steep than the full sample suggests that contaminants in the full sample may be pushing the best fitting power law index higher.

We apply a Kolmogorov-Smirnov test against the mass distribution of M31+M33 J14, and obtain a P-value of 0.02, suggesting only a 2% chance of them having the same parent distribution. Indeed, visually, there is a noticeable difference particularly around $\sim 10 M_{\odot}$ and with more massive progenitors. Thus, the M83 SNR sample really does appear to have more high mass progenitors than those in M31 and M33.

While Figure 6 shows that the M83 distribution is more top-heavy than the M31 and M33 samples, it is still not consistent with a standard IMF (Kroupa 2001); there are too few high mass progenitors for the number at the lower mass end. This result may be due to biases in our technique against the youngest ages dominating the local stellar mass. For exam-

ple, SNe that occur within very young associations, superbubbles, or highly photo-ionized regions may not leave visible SNRs, thus biasing our survey based on optical SNRs. However, there is also a possibility that some fraction of the most massive stars do not explode as SNe. This possibility seems to be corroborated by the discovery of a vanishing red supergiant in NGC 6946 with no observed SN (Adams et al. 2017b; Murphy et al. 2018).

It does appear to be the case that at least some stars $>30 M_{\odot}$ explode as SNe. One such high mass progenitor is that of the SNR 057 (see Figure 5). This case is the highest progenitor mass constraint to date from population fitting techniques. The surrounding population in this case is limited almost entirely to the youngest ages for which we have models, making the progenitor highly likely to have been $>20 M_{\odot}$. This single measurement provides some of our strongest observational evidence to date that such massive stars produce SNe, suggesting that any shortage of progenitor masses $>20 M_{\odot}$ is more likely to be attributable to a bias against young ages or some massive stars failing to explode, rather than to a hard high end cutoff in the progenitor mass distribution. Furthermore, there has been some evidence from stellar population analysis that such high mass progenitors may be more likely to produce stripped envelope SNe (Maud 2018), making SNR 057 a candidate remnant from a stripped envelope event.

4.3. Historical Supernovae

The M83 sample includes six historical supernovae, where the actual explosion was observed. These include SN1923A, SN1945B, SN1950B, SN1957D, SN1968L, and SN1983N. For these, the types are known to be II, unknown, unknown, unknown, II, and Ib, respectively. Thus, the three known types were all core-collapse SNe, which is not surprising given the high star formation rate of M83. Of these, SN1968L occurred deep in the complex nuclear starburst region where its parent population is not resolved even at HST resolution, but the high star formation rate in this region favors a core-collapse event. For SN1923A, we find a likely massive progenitor ($53^{+13}_{-44} M_{\odot}$), as with SN1983N ($20^{+6}_{-5} M_{\odot}$). Of the three unknowns, SN1945B did not have sufficient local stellar photometry for the fit to converge.

SN1950B and SN1957D are candidates for CCSNe progenitors, with masses of $7.6^{+3.3}_{-0.3} M_{\odot}$ and $7.6^{+8.2}_{-0.3} M_{\odot}$ respectively. This measurement for SN1957D is lower than that of Long et al. (2012), who found a lower mass limit of $>17 M_{\odot}$, also looking at the local stellar population. Our analysis detects the presence of two populations at this location: one at an age consistent with the analysis of Long et al. (2012), and an underlying one at ~ 40 -50 Myr, which could have produced a lower-mass progenitor. Thus, this SNR is a good example of why it is important to consider the full

probability distribution, as the single value with uncertainties does not always capture multiple peaks in the age distribution. Interestingly, a similar situation occurs with the SNR 238, which Blair et al. (2015) found to be hosted by a population of very young stars, suggesting a progenitor with a mass $>17 M_{\odot}$. We also detect this young population; however, we also detect a population with an age of 40-50 Myr, making our mass measurement $8.1^{+12.5}_{-0.4} M_{\odot}$. Again, the double-peaked age distribution is important to consider.

Thus, it appears that 5-6 of the 6 historical SNe are core-collapse (with SN1968L very likely core-collapse and SN1945B still unknown), which is similar to the fraction of the total SNR population and roughly consistent with expectations for a Sbc galaxy like M83 ($\sim 20\%$, Li et al. 2011). Furthermore, the 4 historical SNe for which we have measured ages appear to cover the full range of progenitor masses to which we are sensitive.

5. SUMMARY

We measured resolved stellar photometry of seven archival *HST* fields with almost complete coverage of M83. We fit the photometry of stars within a 50 pc of 237 SNRs to derive the age distribution of the populations over the past 50 Myrs. From these age distributions, we inferred probability distributions of 199 of the SNRs' progenitor masses. The other 38 SNRs are good Type Ia candidates as they show no evidence for association with a young population in excess of the general field. The spatial distribution of the 199 progenitor masses show that the most massive progenitors follow the spiral arms and inner disk.

The resulting mass distribution suggests that in M83, as in M31 and M33, the masses are dominated by progenitors

of $<20 M_{\odot}$. There are fewer progenitors with very young ages and high masses than expected from a standard IMF. However, the measurement of some masses above $30 M_{\odot}$, suggests that the low numbers are not due to a high end cut-off in the progenitor mass function. Therefore, they may be due to the difficulty of finding SNRs and measuring resolved stellar photometry in the most dusty and dense star forming regions.

While looking at the overall progenitor mass distributions measured here by using median masses and uncertainties and comparing to simple power-law distributions is of immediate interest for checking consistency with previous work and standard IMFs, we are also performing much more sophisticated statistical fitting of the full probability distributions of the masses (J. Murphy et al. in preparation). By fitting the full probability distributions of the progenitor masses (Table 3) with a reliable likelihood function we will determine the formal constraints on the intrinsic progenitor mass distribution.

Support for this work was provided by NASA through the grant AR-14325 from the Space Telescope Science Institute, which is operated by the Association of Universities for Research in Astronomy, Incorporated, under NASA contract NAS5-26555. Portions of this support were provided to University of Washington (BFW et al.), Johns Hopkins University (WPB), and Eureka Scientific (KSL).

Software: Astrodrizzle (Hack et al. 2012), DOLPHOT (Dolphin 2000, 2016), PyRAF (Science Software Branch at STScI 2012), TinyTim PSFs (Krist et al. 2011a), MATCH (including hybridMC; Dolphin 2002, 2012, 2013)

REFERENCES

- Adams, S. M., Kochanek, C. S., Gerke, J. R., & Stanek, K. Z. 2017a, MNRAS, 469, 1445
- Adams, S. M., Kochanek, C. S., Gerke, J. R., Stanek, K. Z., & Dai, X. 2017b, MNRAS, 468, 4968
- Anderson, J. P., Haberman, S. M., James, P. A., & Hamuy, M. 2012, MNRAS, 424, 1372
- Badenes, C., Harris, J., Zaritsky, D., & Prieto, J. L. 2009, ApJ, 700, 727
- Bastian, N., & Goodwin, S. P. 2006, MNRAS, 369, L9
- Bersten, M. C., Benvenuto, O. G., Folatelli, G., et al. 2014, AJ, 148, 68
- Bianchi, L., Efremova, B., Hodge, P., & Kang, Y. 2012, AJ, 144, 142
- Blair, W. P., & Long, K. S. 2004, ApJS, 155, 101
- Blair, W. P., Winkler, P. F., & Long, K. S. 2012, ApJS, 203, 8
- Blair, W. P., Chandar, R., Dopita, M. A., et al. 2014, ApJ, 788, 55
- Blair, W. P., Winkler, P. F., Long, K. S., et al. 2015, ApJ, 800, 118
- Braun, R., Goss, W. M., & Lyne, A. G. 1989, ApJ, 340, 355
- Bresolin, F., Ryan-Weber, E., Kennicutt, R. C., & Goddard, Q. 2009, ApJ, 695, 580
- Cao, Y., Kasliwal, M. M., Arcavi, I., et al. 2013, ApJL, 775, L7
- Chen, Y., Bressan, A., Girardi, L., et al. 2015, MNRAS, 452, 1068
- Davies, B., & Beasor, E. 2017, ArXiv e-prints, arXiv:1709.06116
- Díaz-Rodríguez, M., Murphy, J. W., Rubin, D. A., et al. 2018, ApJ, 861, 92
- Dolphin, A. 2016, DOLPHOT: Stellar photometry, Astrophysics Source Code Library, ascl:1608.013
- Dolphin, A. E. 2000, PASP, 112, 1383
- . 2002, MNRAS, 332, 91
- . 2012, ApJ, 751, 60
- . 2013, ApJ, 775, 76
- Dopita, M. A., Blair, W. P., Long, K. S., et al. 2010, ApJ, 710, 964

- Eldridge, J. J., & Maund, J. R. 2016, *MNRAS*, 461, L117
- Fremling, C., Sollerman, J., Taddia, F., et al. 2016, *A&A*, 593, A68
- Gallart, C., Zoccali, M., & Aparicio, A. 2005, *ARA&A*, 43, 387
- Girardi, L., Bertelli, G., Bressan, A., et al. 2002, *A&A*, 391, 195
- Girardi, L., Williams, B. F., Gilbert, K. M., et al. 2010, *ApJ*, 724, 1030
- Gogarten, S. M., Dalcanton, J. J., Murphy, J. W., et al. 2009, *ApJ*, 703, 300
- Groh, J. H., Georgy, C., & Ekström, S. 2013, *A&A*, 558, L1
- Guillochon, J., Parrent, J., Kelley, L. Z., & Margutti, R. 2017, *ApJ*, 835, 64
- Hack, W. J., Dencheva, N., Fruchter, A. S., et al. 2012, in *American Astronomical Society Meeting Abstracts*, Vol. 220, *American Astronomical Society Meeting Abstracts #220*, 135.15
- Jennings, Z. G., Williams, B. F., Murphy, J. W., et al. 2012, *ApJ*, 761, 26
- . 2014, *ApJ*, 795, 170
- Kang, Y., Bianchi, L., & Rey, S.-C. 2009, *ApJ*, 703, 614
- Kilpatrick, C. D., Takaro, T., Foley, R. J., et al. 2018, *MNRAS*, 480, 2072
- Kim, H., Whitmore, B. C., Chandar, R., et al. 2012, *ApJ*, 753, 26
- Krist, J. E., Hook, R. N., & Stoehr, F. 2011a, in *Proc. SPIE*, Vol. 8127, *Optical Modeling and Performance Predictions V*, 81270J
- Krist, J. E., Hook, R. N., & Stoehr, F. 2011b, in *Proc. SPIE*, Vol. 8127, *Optical Modeling and Performance Predictions V*, 81270J
- Kroupa, P. 2001, *MNRAS*, 322, 231
- Lada, C. J., & Lada, E. A. 2003, *ARA&A*, 41, 57
- Li, W., Chornock, R., Leaman, J., et al. 2011, *MNRAS*, 412, 1473
- Long, K. S., Kuntz, K. D., Blair, W. P., et al. 2014, *ApJS*, 212, 21
- Long, K. S., Blair, W. P., Godfrey, L. E. H., et al. 2012, *ApJ*, 756, 18
- Lundgren, A. A., Olofsson, H., Wiklund, T., & Rydbeck, G. 2004, *A&A*, 422, 865
- Marigo, P., Girardi, L., Bressan, A., et al. 2008, *A&A*, 482, 883
- Maund, J. R. 2018, *MNRAS*, 476, 2629
- McQuinn, K. B. W., Skillman, E. D., Cannon, J. M., et al. 2010, *ApJ*, 721, 297
- Murphy, J. W., Jennings, Z. G., Williams, B., Dalcanton, J. J., & Dolphin, A. E. 2011, *ApJL*, 742, L4
- Murphy, J. W., Khan, R., Williams, B., et al. 2018, *ApJ*, 860, 117
- Richter, O.-G., & Rosa, M. 1984, *A&A*, 140, L1
- Saha, A., Thim, F., Tammann, G. A., Reindl, B., & Sandage, A. 2006, *ApJS*, 165, 108
- Schlafly, E. F., & Finkbeiner, D. P. 2011, *ApJ*, 737, 103
- Science Software Branch at STScI. 2012, *PyRAF: Python alternative for IRAF*, *Astrophysics Source Code Library*, ascl:1207.011
- Senchyna, P., Johnson, L. C., Dalcanton, J. J., et al. 2015, *ApJ*, 813, 31
- Skillman, E. D., Monelli, M., Weisz, D. R., et al. 2017, *ApJ*, 837, 102
- Smartt, S. J. 2009, *ARA&A*, 47, 63
- . 2015, *PASA*, 32, e016
- Smartt, S. J., Eldridge, J. J., Crockett, R. M., & Maund, J. R. 2009, *MNRAS*, 395, 1409
- Van Dyk, S. D. 2017, *Philosophical Transactions of the Royal Society of London Series A*, 375, 20160277
- Van Dyk, S. D., Zheng, W., Brink, T. G., et al. 2018, *ApJ*, 860, 90
- Weisz, D. R., Dalcanton, J. J., Williams, B. F., et al. 2011, *ApJ*, 739, 5
- Williams, B. F., Dalcanton, J. J., Dolphin, A. E., Holtzman, J., & Sarajedini, A. 2009, *ApJL*, 695, L15
- Williams, B. F., Hillis, T. J., Murphy, J. W., et al. 2018, *ApJ*, 860, 39
- Williams, B. F., Peterson, S., Murphy, J., et al. 2014a, *ApJ*, 791, 105
- Williams, B. F., Lang, D., Dalcanton, J. J., et al. 2014b, *ApJS*, 215, 9
- Williams, B. F., Dolphin, A. E., Dalcanton, J. J., et al. 2017, *ApJ*, 846, 145
- Winkler, P. F., Blair, W. P., & Long, K. S. 2017, *ApJ*, 839, 83
- Xiang, D., Wang, X., Mo, J., et al. 2019, *ApJ*, 871, 176
- Xiao, L., Galbany, L., Eldridge, J. J., & Stanway, E. R. 2019, *MNRAS*, 482, 384

Table 1. M83 Supernova Remnants

Source ID	B12	B14	D10	L14	RA	DEC	Quality Flag	Use Flag
001	B12-001	–	–	–	204.166625	-29.859764	1b	o
002	B12-002	–	–	–	204.168112	-29.851814	2	o
003	B12-003	–	–	X019	204.1704	-29.854906	1a	o
004	B12-004	–	–	–	204.172921	-29.871072	1c	o
005	B12-005	–	–	–	204.173246	-29.8323	1b	o
006	B12-006	–	–	–	204.176375	-29.871492	1c	o
007	B12-007	–	–	–	204.178012	-29.876375	1c	o
008	B12-008	–	–	–	204.182079	-29.846078	1c	o
009	B12-009	–	–	–	204.182579	-29.869775	1c	o
010	B12-010	–	–	–	204.186	-29.842747	1b	o
011	B12-011	–	–	–	204.1888	-29.885486	1c	o
012	B12-012	–	–	–	204.190258	-29.872578	1b	o
013	B12-013	–	–	–	204.191375	-29.892878	1c	o
014	B12-014	–	–	–	204.1934	-29.895092	2	o
015	B12-015	–	–	–	204.195592	-29.778244	2	o
016	B12-016	–	–	–	204.196371	-29.925422	2	o
017	B12-017	–	–	–	204.196583	-29.897611	2	o
018	B12-018	–	–	–	204.196758	-29.893589	1c	o
019	B12-019	–	–	–	204.197083	-29.817708	1c	o
020	B12-020	–	–	–	204.199279	-29.855039	1b	i
021	B12-021	–	–	–	204.199721	-29.862778	2	i
022	B12-307	–	–	–	204.199958	-29.890722	2	o
023	B12-022	–	–	–	204.200446	-29.859408	1b	n
024	B12-023	–	–	X046	204.201233	-29.879075	1a	p
025	B12-024	–	–	–	204.201883	-29.861719	1c	n
026	B12-025	–	–	–	204.20245	-29.868144	1b	n
027	B12-026	B14-01	–	–	204.204138	-29.881692	1b	p
028	B12-027	–	–	–	204.204688	-29.873583	1c	p
029	B12-028	–	–	–	204.205692	-29.888867	2	p
030	B12-029	–	–	–	204.206408	-29.8603	2	p
031	B12-030	–	–	–	204.206687	-29.884908	1c	p
032	B12-031	–	–	–	204.206762	-29.887125	1b	p
033	B12-32	–	–	–	204.2068	-29.8429	2	p
034	B12-033	–	–	–	204.207004	-29.901153	1b	p
035	B12-034	–	–	–	204.207158	-29.849208	1b	p

Table 1 continued

Table 1 (*continued*)

Source ID	B12	B14	D10	L14	RA	DEC	Quality Flag	Use Flag
036	B12-036	B14-02	–	X053	204.207538	-29.871375	1a	p
037	B12-035	–	–	-	204.207546	-29.885639	1b	n
038	B12-309	–	–	-	204.207896	-29.883083	2	n
039	–	B14-03	–	-	204.208817	-29.878797	1g	p
040	B12-037	B14-04	–	X057	204.208821	-29.88575	1a	p
041	B12-038	–	–	-	204.209292	-29.856747	1c	i
042	B12-310	–	–	-	204.209333	-29.843581	2	p
043	B12-039	–	–	-	204.209517	-29.879861	1b	p
044	B12-040	–	–	-	204.210408	-29.863831	1c	p
045	B12-041	B14-05	–	X061	204.210633	-29.884411	1d	p
046	B12-042	–	–	-	204.211204	-29.878206	2	p
047	B12-043	–	–	-	204.211492	-29.886275	1b	p
048	B12-044	–	–	-	204.211704	-29.838556	2	p
049	B12-045	–	–	X063	204.211896	-29.877658	1a	p
SN1983N	–	–	–	-	204.21204	-29.901278	h	p
051	B12-047	–	–	X064	204.212154	-29.882981	1d	p
052	B12-046	–	–	-	204.212167	-29.867728	1c	p
053	B12-048	–	–	X065	204.212475	-29.873872	1a	p
054	B12-049	B14-06	–	-	204.212579	-29.883711	2	p
055	–	B14-07	–	X067	204.2133	-29.845089	1e	p
056	B12-050	–	–	-	204.213458	-29.877964	2	p
057	B12-051	–	–	-	204.213825	-29.835297	2	p
058	B12-052	–	–	-	204.214292	-29.824497	1c	p
059	–	B14-08	–	-	204.214512	-29.8759	1g	p
060	–	B14-09	–	-	204.214692	-29.883589	2	p
061	B12-053	–	–	-	204.214942	-29.880575	1c	p
062	B12-054	–	–	-	204.215421	-29.874344	2	p
063	–	B14-10	–	-	204.215858	-29.867194	1g	p
064	B12-55	–	–	-	204.216562	-29.914561	1c	p
065	B12-311	–	–	-	204.217796	-29.905803	2	n
066	B12-056	–	–	-	204.218092	-29.842544	1c	n
067	B12-058	–	–	-	204.218258	-29.868097	2	n
068	B12-057	–	–	-	204.218321	-29.845536	1b	p
069	B12-059	–	–	-	204.2188	-29.825731	2	p
070	B12-060	–	–	X093	204.219329	-29.8782	1d	p
071	B12-061	–	–	-	204.219904	-29.857919	2	p
SN1950B	–	–	–	-	204.22071	-29.865861	h	p

Table 1 continued

Table 1 (*continued*)

Source ID	B12	B14	D10	L14	RA	DEC	Quality Flag	Use Flag
073	B12-062	–	–	-	204.220771	-29.839964	1c	i
074	B12-063	–	–	-	204.221183	-29.871217	1d	p
075	B12-064	–	–	-	204.221587	-29.874806	2	n
076	B12-065	B14-11	–	X105	204.221783	-29.890369	1a	p
077	B12-067	B14-12	–	X106	204.222046	-29.88005	1a	p
078	B12-066	–	–	X107	204.222062	-29.878478	1a	n
079	B12-068	–	–	-	204.222179	-29.930956	2	o
080	B12-069	–	–	-	204.222367	-29.843989	1b	n
081	B12-070	–	–	-	204.222967	-29.877269	1c	n
SN1945B	–	–	–	-	204.223335	-29.915556	h	i
083	B12-312	–	–	X110	204.223337	-29.933567	1e	o
084	B12-071	–	–	-	204.223446	-29.879417	1c	n
085	–	B14-13	–	-	204.223871	-29.814239	2	p
086	B12-072	–	–	-	204.224054	-29.91135	1c	n
087	B12-073	–	–	X116	204.224558	-29.813383	1a	p
088	B12-074	–	–	X119	204.225671	-29.86925	1a	p
089	B12-075	B14-14	–	X121	204.226012	-29.841156	1d	p
090	B12-076	–	–	-	204.226433	-29.838208	1c	p
091	B12-077	–	–	-	204.226858	-29.933436	1f	o
092	B12-078	–	–	-	204.226937	-29.848047	2	p
093	B12-079	–	–	-	204.227054	-29.84065	1c	p
094	B12-080	–	–	-	204.227608	-29.884706	2	p
095	B12-081	–	–	-	204.227646	-29.883658	2	p
096	B12-082	–	–	X127	204.2283	-29.883167	1d	p
097	B12-083	–	–	-	204.228442	-29.884647	2	p
098	B12-085	–	–	-	204.228521	-29.831553	2	p
099	B12-084	–	–	X128	204.228617	-29.838492	1a	p
100	B12-086	–	–	-	204.228917	-29.796075	2	o
101	B12-088	–	–	-	204.229304	-29.856922	1c	p
102	B12-087	–	–	X129	204.229312	-29.877658	1a	n
103	B12-313	–	–	-	204.229371	-29.915103	2	p
104	B12-089	–	–	X131	204.229437	-29.884578	1a	p
105	B12-090	–	–	X134	204.229692	-29.844531	1d	p
106	B12-091	–	–	-	204.230075	-29.884717	1b	p
107	B12-314	B14-15	–	-	204.230312	-29.900789	2	p
108	B12-092	–	–	-	204.230471	-29.843678	1c	p
109	B12-094	–	–	-	204.230513	-29.832406	2	p

Table 1 continued

Table 1 (*continued*)

Source ID	B12	B14	D10	L14	RA	DEC	Quality Flag	Use Flag
110	B12-093	–	–	X136	204.230638	-29.848253	1d	p
111	B12-95	–	–	-	204.230858	-29.810886	1c	p
112	B12-096	–	–	-	204.231125	-29.884297	1c	p
113	B12-097	–	–	-	204.231146	-29.878808	1b	p
114	B12-098	–	–	-	204.231729	-29.884336	1b	p
115	B12-099	–	–	-	204.231729	-29.793711	2	o
116	B12-100	–	–	-	204.232054	-29.823644	2	p
117	B12-101	–	–	-	204.232492	-29.855483	1b	p
118	B12-102	–	–	-	204.232625	-29.885894	2	p
119	B12-103	–	–	-	204.232967	-29.886375	1c	p
120	B12-104	–	–	-	204.2336	-29.934903	1b	o
121	B12-105	–	–	-	204.233779	-29.826392	2	p
122	B12-106	B14-16	–	X141	204.234279	-29.881994	1a	n
123	B12-107	–	–	-	204.234479	-29.887067	1c	p
124	B12-108	–	–	-	204.234842	-29.825644	2	p
125	B12-109	B14-17	–	X149	204.2367	-29.830461	1a	p
126	B12-110	–	–	-	204.236742	-29.823558	1b	p
127	B12-111	–	–	-	204.237183	-29.902956	1c	n
128	B12-112	–	–	-	204.238154	-29.892706	1b	p
129	B12-113	–	–	-	204.240975	-29.801625	2	p
130	B12-115	B14-18	–	X159	204.241167	-29.884097	1a	p
131	B12-114	–	–	-	204.241525	-29.803514	1c	p
132	B12-316	–	–	-	204.241833	-29.817222	2	o
133	B12-116	–	–	-	204.241975	-29.8958	1c	p
134	B12-117	–	–	X166	204.243971	-29.805475	1e	p
135	–	B14-19	–	-	204.244346	-29.851803	1b	p
136	B12-118	–	D10-01	X172	204.244683	-29.850156	1a	n
137	–	B14-20	D10-02	-	204.245412	-29.873961	1b	p
138	B12-119	B14-21	–	-	204.245837	-29.882442	2	p
139	B12-120	–	–	-	204.245854	-29.883708	1c	p
140	B12-318	–	–	-	204.24595	-29.916283	2	i
141	B12-121	–	–	-	204.246271	-29.895386	2	p
142	–	B14-22	D10-03	X181	204.246537	-29.863306	1d	n
143	B12-319	–	–	-	204.247079	-29.916158	2	p
144	–	B14-23	–	-	204.24715	-29.810142	2	p
145	B12-122	–	–	X183	204.247217	-29.919153	1a	p
146	B12-123	–	–	X184	204.247262	-29.810469	1d	p

Table 1 continued

Table 1 (*continued*)

Source ID	B12	B14	D10	L14	RA	DEC	Quality Flag	Use Flag
147	–	B14-24	–	-	204.247675	-29.810275	2	p
148	B12-320	–	–	-	204.247687	-29.909628	2	n
149	B12-125	–	–	-	204.247796	-29.821292	1b	n
150	B12-124	–	D10-04	X186	204.247933	-29.867761	1a	p
151	B12-126	–	D10-05	-	204.248683	-29.842431	1c	n
152	–	B14-25	–	-	204.249121	-29.810519	2	p
153	B12-127	–	–	X195	204.249371	-29.923881	1a	i
154	B12-128	–	–	-	204.250042	-29.809369	1c	n
155	B12-129	B14-26	–	X199	204.250137	-29.904708	1a	n
156	–	B14-27	D10-N-01	X202	204.250188	-29.867206	1d	c
157	–	B14-28	D10-06	-	204.250271	-29.869097	1c	c
158	B12-130	–	–	-	204.250354	-29.811194	2	p
159	B12-131	–	–	X205	204.250654	-29.802817	1d	p
160	–	–	D10-N-02	-	204.250883	-29.866214	1h	c
161	B12-132	–	D10-07	-	204.2514	-29.855756	1b	n
162	–	–	D10-N-05	-	204.251608	-29.866303	1c	c
SN1968L	–	–	–	-	204.251625	-29.866250	h	c
164	–	–	D10-N-06	-	204.251654	-29.867142	1h	c
165	B12-133	–	–	X215	204.251654	-29.889697	1a	p
166	–	B14-30	D10-N-07	-	204.251725	-29.868392	1h	c
167	–	B14-31	–	-	204.251729	-29.872931	1c	p
168	–	B14-32	–	-	204.252292	-29.868486	2	c
169	–	–	D10-N-08	-	204.252308	-29.866319	1c	c
170	–	–	D10-N-09	-	204.252496	-29.869111	1h	c
171	–	–	D10-N-10	-	204.252692	-29.866497	1h	c
172	B12-134	–	–	-	204.252817	-29.907414	1b	p
173	–	–	D10-N-11	-	204.252825	-29.865856	1h	c
174	B12-135	–	D10-08	-	204.252854	-29.872781	2	p
175	–	–	D10-N-12	-	204.252938	-29.866636	1h	c
176	B12-136	–	–	-	204.253062	-29.889928	2	p
177	–	–	D10-N-13	-	204.253171	-29.868306	1h	c
178	–	B14-34	–	-	204.25365	-29.869014	2	c
179	–	–	D10-N-14	-	204.253892	-29.865042	1h	c
180	–	–	D10-N-14	-	204.253896	-29.865181	1g	c
181	–	–	D10-N-15	-	204.253933	-29.865522	1h	c
182	–	–	D10-N-14	-	204.254054	-29.864886	1g	c
183	B12-137	B14-35	D10-09	X235	204.254238	-29.848983	1a	p

Table 1 continued

Table 1 (*continued*)

Source ID	B12	B14	D10	L14	RA	DEC	Quality Flag	Use Flag
184	B12-138	–	–	-	204.254425	-29.904408	1c	p
185	–	B14-36	D10-10	-	204.254463	-29.861544	2	p
186	–	–	D10-N-16	-	204.254646	-29.86445	1z	c
187	B12-139	–	–	-	204.254817	-29.952981	1c	o
188	–	–	D10-N-17	X241	204.254892	-29.865928	1d	c
189	B12-321	B14-38	–	X243	204.255313	-29.866636	1z	c
190	–	–	D10-N-18	-	204.255479	-29.865956	1h	c
191	B12-140	–	–	-	204.256304	-29.837425	1c	n
192	B12-141	–	–	X249	204.25645	-29.833019	1d	p
193	–	B14-39	D10-N-19	X250	204.256717	-29.867206	1d	c
194	B12-142	–	–	X253	204.256933	-29.902803	1a	p
195	B12-143	–	D10-12	X256	204.257133	-29.853711	1d	p
196	B12-144	–	–	X255	204.257167	-29.911217	1d	p
197	–	B14-37	–	-	204.258308	-29.864289	1g	p
198	B12-145	–	D10-13	-	204.258492	-29.880444	1c	p
199	B12-146	–	D10-14	-	204.258612	-29.866197	1b	p
200	B12-147	B14-40	–	X261	204.2592	-29.831231	1a	i
201	B12-148	–	–	X262	204.25965	-29.835272	1a	p
202	B12-149	–	–	-	204.260058	-29.90915	1c	p
203	B12-150	B14-41	D10-15	X265	204.260096	-29.857236	1a	p
204	–	B14-42	–	-	204.262033	-29.810861	2	p
205	B12-151	B14-43	–	X272	204.262563	-29.829294	1e	p
206	–	B14-44	–	-	204.263096	-29.9047	1g	n
207	–	B14-45	–	-	204.264183	-29.900689	1g	p
208	B12-152	–	–	-	204.264512	-29.846303	2	p
SN1957D	B12-324	B14-46	–	X279	204.264917	-29.827981	h	p
210	B12-153	–	–	-	204.266167	-29.828614	2	p
211	B12-154	–	–	-	204.2669	-29.900539	1b	p
212	–	–	D10-1-01	-	204.267158	-29.851053	2	n
213	B12-155	–	–	-	204.267242	-29.887847	1b	p
214	B12-156	–	–	X287	204.268383	-29.827403	1a	p
215	B12-158	–	–	-	204.268533	-29.900939	2	p
216	B12-157	–	–	-	204.268596	-29.896589	1b	p
217	B12-159	–	–	X288	204.26875	-29.826542	1a	p
218	B12-160	–	–	X292	204.269638	-29.926342	1a	n
219	B12-161	–	–	-	204.269833	-29.898228	2	p
220	B12-162	–	–	-	204.270054	-29.835219	1b	p

Table 1 continued

Table 1 (*continued*)

Source ID	B12	B14	D10	L14	RA	DEC	Quality Flag	Use Flag
221	B12-163	–	–	-	204.2702	-29.828344	2	n
222	–	–	D10-17	-	204.270321	-29.871828	1b	n
223	B12-164	–	–	-	204.270683	-29.837872	1c	n
224	–	B14-47	–	-	204.270933	-29.922703	1g	p
225	B12-165	–	–	-	204.273271	-29.915633	1c	p
226	B12-166	–	D10-18	-	204.274162	-29.879456	1c	n
227	B12-167	–	–	-	204.274462	-29.917772	2	p
228	–	B14-49	–	-	204.2745	-29.845961	2	p
229	B12-327	–	–	-	204.274504	-29.819794	2	p
230	B12-168	–	–	-	204.275004	-29.834508	1b	p
231	B12-169	–	–	X310	204.275146	-29.920647	1a	p
232	B12-170	–	–	X311	204.275671	-29.912089	1a	i
233	–	B14-50	–	-	204.275971	-29.918081	2	p
234	B12-171	–	D10-19	X313	204.276821	-29.840269	1a	p
235	B12-172	–	–	-	204.276854	-29.907578	1b	p
236	B12-173	–	–	-	204.276854	-29.835061	1c	p
237	B12-174	–	–	-	204.277688	-29.892786	1c	p
238	B12-174a	–	–	X316	204.277692	-29.892392	1z	p
239	B12-175	–	–	-	204.278433	-29.823953	2	p
240	–	–	D10-1-02	-	204.279042	-29.849206	2	p
241	B12-328	–	–	-	204.279046	-29.915914	2	p
242	–	B14-51	D10-20	-	204.279121	-29.852664	2	p
243	B12-177	–	–	X319	204.279142	-29.818856	1d	p
244	B12-176	–	–	-	204.279171	-29.904494	1c	n
245	B12-178	–	–	X320	204.279496	-29.889158	1a	p
246	B12-329	–	–	-	204.279546	-29.820414	2	p
247	B12-179	B14-52	–	-	204.279604	-29.850431	1b	p
248	B12-180	–	D10-22	X326	204.281129	-29.859267	1a	p
249	B12-181	–	–	-	204.28125	-29.904494	1b	n
250	B12-182	–	D10-23	-	204.281538	-29.872003	1c	n
251	B12-183	B14-53	D10-21	-	204.282038	-29.852792	1f	p
252	B12-184	–	–	-	204.282113	-29.883692	1b	p
253	B12-185	–	–	-	204.282488	-29.9034	1b	p
254	B12-186	–	–	X330	204.283	-29.822253	1d	p
255	B12-187	–	–	-	204.283375	-29.854592	2	p
256	B12-188	–	D10-25	-	204.283746	-29.872636	1b	p
257	B12-189	–	–	-	204.283983	-29.889078	2	p

Table 1 continued

Table 1 (*continued*)

Source ID	B12	B14	D10	L14	RA	DEC	Quality Flag	Use Flag
258	–	B14-54	D10-26	X336	204.284713	-29.848981	1a	p
259	–	B14-55	–	-	204.284983	-29.879919	2	p
260	–	B14-56	–	-	204.285096	-29.869508	2	p
261	B12-190	–	D10-27	-	204.285333	-29.867222	1d	p
262	B12-191	–	D10-28	X339	204.285696	-29.859772	1a	p
263	B12-333	B14-57	D10-29	X341	204.285983	-29.878556	1e	p
264	B12-192	–	D10-30	-	204.286025	-29.864828	1c	p
265	B12-193	–	D10-32	X342	204.286496	-29.860425	1a	p
266	B12-194	–	D10-33	-	204.287708	-29.859261	1b	p
SN1923A	–	–	–	-	204.28827	-29.850386	h	p
268	B12-195	–	D10-34	X348	204.288446	-29.859433	1d	p
269	–	B14-58	D10-35	-	204.288813	-29.849592	2	p
270	B12-196	–	–	-	204.290363	-29.891717	1c	p
271	B12-197	–	D10-36	X350	204.291992	-29.857828	1a	p
272	B12-198	–	–	-	204.292454	-29.838372	2	p
273	B12-334	–	–	-	204.292475	-29.816472	2	p
274	B12-199	–	D10-37	X352	204.292963	-29.858058	1a	p
275	–	–	D10-38	-	204.293183	-29.859425	1b	p
276	B12-200	–	–	-	204.294921	-29.832372	2	p
277	B12-201	–	D10-39	-	204.294996	-29.862403	1b	p
278	–	–	D10-40	-	204.295163	-29.879019	1b	p
279	B12-202	–	–	-	204.295525	-29.831381	1b	p
280	B12-203	–	–	X353	204.295708	-29.8462	1d	p
281	B12-204	–	–	-	204.296283	-29.888086	1b	n
282	B12-205	–	–	-	204.297229	-29.905403	2	p
283	B12-207	–	–	X355	204.297771	-29.837117	1a	p
284	B12-206	–	–	X356	204.297808	-29.861489	1a	p
285	B12-208	–	–	-	204.29845	-29.860981	2	p
286	B12-209	–	–	-	204.299483	-29.871036	1a	p
287	B12-336	B14-59	–	X360	204.30035	-29.849208	1e	p
288	B12-210	–	–	X364	204.3019	-29.838903	1a	o
289	B12-211	–	–	X368	204.303367	-29.836678	1a	o
290	B12-338	–	–	-	204.303392	-29.9123	2	i
291	B12-212	–	–	-	204.303517	-29.910761	1c	n
292	–	B14-60	–	-	204.304442	-29.860683	2	p
293	B12-213	–	–	-	204.304488	-29.855053	1b	p
294	–	B14-61	–	-	204.305525	-29.859972	2	p

Table 1 continued

Table 1 (*continued*)

Source ID	B12	B14	D10	L14	RA	DEC	Quality Flag	Use Flag
295	B12-215	–	–	-	204.308208	-29.864208	1b	p
296	B12-214	–	–	-	204.308442	-29.881753	1c	p
297	B12-216	–	–	-	204.309812	-29.8351	1c	o
298	B12-217	–	–	-	204.310125	-29.839233	1c	p
299	B12-218	–	–	-	204.311167	-29.842789	2	p
300	B12-219	–	–	-	204.311829	-29.916283	1b	o
301	B12-220	–	–	-	204.316771	-29.884439	1b	o
302	B12-221	B14-62	–	X389	204.321675	-29.864825	1a	p
303	B12-222	–	–	-	204.321942	-29.890267	1b	o
304	B12-223	B14-63	–	X391	204.322612	-29.864969	1a	p
305	B12-224	–	–	-	204.322892	-29.893278	1c	o
306	B12-344	–	–	-	204.324125	-29.865397	2	p
307	B12-225	–	–	-	204.328079	-29.897375	1c	o

Table 2. SNR photometry depth, extinction, and progenitor mass estimates

ID	50% Completeness Limit			Count _{F438W}	dAv	Av	M_{ZAMS}
	F336W	F438W	F814W				
024	26.0	27.0	25.9	425	0.0	0.2	14.86 ^{+0.84} _{-1.46}
027	26.2	27.2	26.1	173	0.0	1.6	8.43 ^{+1.87} _{-0.73}
028	26.0	27.0	25.8	64	0.0	1.8	11.37 ^{+4.33} _{-4.07}
029	26.3	27.1	26.1	150	0.0	0.2	8.07 ^{+4.43} _{-0.37}
030	26.1	27.0	26.0	98	0.4	0.8	7.64 ^{+5.76} _{-0.34}
031	25.9	26.8	25.3	57	0.4	1.2	9.94 ^{+1.76} _{-2.24}
032	26.3	27.1	26.0	187	0.0	0.2	9.90 ^{+7.20} _{-1.30}
033	26.3	27.1	26.1	149	0.0	0.2	9.93 ^{+3.47} _{-0.93}
034	25.9	26.8	25.3	47	0.0	1.2	43.16 ^{+8.94} _{-34.16}
035	26.0	27.0	25.8	52	0.0	0.4	27.14 ^{+2.06} _{-17.54}
036	26.3	27.1	26.0	177	0.0	0.6	9.50 ^{+3.90} _{-0.50}
039	26.1	27.0	25.9	203	1.6	0.8	12.17 ^{+4.93} _{-2.57}
040	26.0	26.7	25.1	40	0.0	2.4	15.10 ^{+8.00} _{-7.80}
042	26.3	27.0	26.0	190	0.6	0.6	9.56 ^{+2.14} _{-0.56}
043	26.1	27.0	25.9	222	0.0	0.2	10.86 ^{+0.84} _{-0.56}
044	26.0	26.9	25.5	105	0.0	0.2	9.73 ^{+3.67} _{-0.73}
045	26.0	26.9	25.5	125	0.2	0.8	10.65 ^{+1.85} _{-1.65}
046	26.2	26.9	26.0	161	0.6	1.0	16.78 ^{+1.92} _{-5.88}

Table 2 continued

Table 2 (*continued*)

ID	50% Completeness Limit			Count _{F438W}	dAv	Av	M_{ZAMS}
	F336W	F438W	F814W				
047	26.0	27.1	25.8	86	0.0	1.2	8.80 ^{+5.70} _{-0.70}
048	26.0	27.0	25.8	54	0.0	0.4	8.53 ^{+3.97} _{-0.43}
049	26.3	27.3	26.3	136	0.4	1.0	11.29 ^{+2.11} _{-0.99}
051	26.3	27.1	26.1	162	0.8	1.0	8.98 ^{+3.52} _{-0.38}
052	25.8	26.5	25.2	770	0.6	0.2	10.68 ^{+5.02} _{-0.38}
053	25.5	26.4	25.5	894	2.2	0.2	18.40 ^{+0.30} _{-6.70}
054	26.3	27.1	26.1	175	0.0	0.6	11.17 ^{+3.33} _{-2.57}
055	26.3	27.1	26.0	120	0.6	1.0	21.22 ^{+1.88} _{-11.62}
056	26.1	27.0	25.9	183	1.0	0.8	10.09 ^{+8.61} _{-0.49}
057	26.3	27.0	26.0	131	0.4	0.4	59.00 ^{+7.60} _{-38.40}
058	26.0	27.1	25.8	41	0.0	1.0	9.33 ^{+9.37} _{-0.73}
059	26.0	26.7	25.1	36	0.2	2.6	16.77 ^{+0.33} _{-7.77}
060	25.9	26.9	25.8	144	0.8	1.2	21.49 ^{+1.61} _{-13.39}
061	26.3	27.1	26.1	190	0.0	0.6	9.56 ^{+1.34} _{-0.56}
062	26.0	26.9	25.7	205	0.0	1.0	11.80 ^{+1.60} _{-2.80}
063	26.1	27.0	26.0	187	0.0	0.8	7.53 ^{+4.17} _{-0.23}
064	25.9	26.8	25.3	41	0.0	0.4	27.56 ^{+1.64} _{-15.86}
068	26.5	27.3	26.3	65	0.0	2.0	12.06 ^{+0.44} _{-4.76}
069	26.0	27.1	25.8	41	0.0	0.6	7.93 ^{+7.77} _{-0.23}
070	26.0	26.8	25.9	384	0.0	0.2	8.02 ^{+2.28} _{-0.32}
071	26.0	27.0	25.9	199	0.0	0.6	8.97 ^{+5.53} _{-0.37}
074	26.1	27.1	25.9	170	0.2	0.2	9.94 ^{+5.76} _{-0.34}
076	25.5	26.4	25.5	342	0.8	0.2	14.66 ^{+4.04} _{-3.76}
077	25.9	26.9	25.9	593	2.2	0.6	7.71 ^{+3.99} _{-0.41}
085	25.8	26.5	25.2	180	0.0	0.2	22.24 ^{+12.46} _{-11.94}
087	26.0	26.9	26.1	274	0.8	0.2	16.23 ^{+12.97} _{-6.63}
088	26.1	27.1	25.8	78	0.0	2.8	7.53 ^{+27.17} _{-0.23}
089	26.2	26.9	26.0	298	1.0	0.4	10.77 ^{+7.93} _{-0.47}
090	26.2	27.2	26.1	35	0.0	2.0	9.33 ^{+11.27} _{-0.73}
092	26.1	27.1	25.9	133	0.0	1.6	12.09 ^{+2.41} _{-4.39}
093	26.0	26.9	25.5	97	0.2	1.0	9.96 ^{+0.34} _{-0.36}
094	26.3	27.0	26.0	181	0.8	1.0	9.45 ^{+3.95} _{-0.45}
095	26.1	27.1	25.9	132	0.0	1.2	9.40 ^{+1.50} _{-0.80}
096	26.0	27.0	25.9	208	3.0	1.2	10.92 ^{+0.78} _{-2.82}
097	26.1	27.1	25.9	220	2.0	0.2	11.03 ^{+0.67} _{-1.43}
098	26.3	27.3	26.3	153	0.0	0.2	7.55 ^{+4.95} _{-0.25}

Table 2 continued

Table 2 (*continued*)

ID	50% Completeness Limit			Count _{F438W}	dAv	Av	M_{ZAMS}
	F336W	F438W	F814W				
099	26.5	27.3	26.3	78	0.0	2.0	$7.93^{+15.17}_{-0.63}$
101	26.0	27.1	25.8	82	0.0	1.6	$15.06^{+0.64}_{-7.76}$
103	25.9	26.8	25.3	39	0.0	1.8	$10.60^{+5.10}_{-3.30}$
104	26.0	26.9	25.5	110	0.6	1.2	$11.26^{+1.24}_{-2.66}$
105	26.3	27.0	26.0	225	0.2	0.6	$8.77^{+2.93}_{-0.17}$
106	26.1	27.1	25.9	137	0.0	1.4	$10.64^{+1.06}_{-2.54}$
107	26.0	26.9	25.7	266	2.0	0.8	$8.73^{+2.17}_{-0.13}$
108	26.1	27.0	25.9	251	0.0	0.4	$11.74^{+1.66}_{-3.64}$
109	26.1	27.0	26.0	120	0.0	0.2	$9.91^{+5.79}_{-0.91}$
110	26.3	27.1	26.0	182	0.0	0.8	$8.35^{+7.35}_{-0.25}$
111	26.1	27.1	25.8	51	0.0	1.4	$8.35^{+5.05}_{-0.65}$
112	26.1	27.0	26.0	149	0.4	1.6	$14.12^{+0.38}_{-6.42}$
113	26.0	26.7	25.1	46	0.0	1.6	$8.35^{+3.35}_{-0.65}$
114	26.3	27.1	26.1	205	0.0	0.8	$8.88^{+3.62}_{-0.28}$
116	26.0	27.0	25.8	71	0.0	0.8	$8.74^{+0.86}_{-0.14}$
117	26.2	27.2	26.1	102	0.0	0.8	$8.35^{+8.75}_{-0.25}$
118	26.0	26.9	25.7	166	1.6	1.0	$19.92^{+0.68}_{-9.02}$
119	26.2	26.9	26.0	169	1.4	0.8	$12.45^{+4.65}_{-0.75}$
121	26.3	27.1	26.1	168	0.0	0.8	$8.52^{+4.88}_{-0.42}$
123	25.9	26.8	25.3	59	0.0	1.0	$9.33^{+1.57}_{-0.73}$
124	25.9	26.9	25.8	151	0.0	0.6	$13.59^{+0.91}_{-4.59}$
125	26.2	27.2	26.1	100	0.0	0.6	$13.16^{+1.34}_{-2.26}$
126	26.0	26.7	25.1	45	0.0	0.6	$9.93^{+4.57}_{-0.93}$
128	25.9	26.8	25.3	62	0.0	2.0	$12.07^{+8.53}_{-4.77}$
129	26.0	26.7	25.1	40	0.0	0.8	$14.58^{+1.12}_{-5.58}$
130	26.1	27.1	25.9	133	0.8	1.8	$8.38^{+4.12}_{-1.08}$
131	26.0	27.1	25.8	52	0.0	1.4	$10.05^{+2.45}_{-2.35}$
133	26.0	26.8	25.9	338	0.0	0.2	$8.48^{+1.82}_{-0.38}$
134	26.1	27.0	25.9	144	0.0	0.2	$20.31^{+2.79}_{-4.61}$
135	26.1	27.1	25.9	125	0.0	0.4	$18.93^{+1.67}_{-9.33}$
137	26.2	27.2	26.1	107	0.0	1.6	$9.85^{+1.05}_{-2.15}$
138	26.3	27.3	26.3	142	0.0	1.8	$19.66^{+0.94}_{-11.96}$
139	26.0	26.8	25.9	302	0.8	0.2	$14.15^{+2.95}_{-0.75}$
141	25.5	26.4	25.5	295	2.6	0.6	$8.01^{+0.99}_{-0.31}$
143	26.2	27.2	26.1	86	0.0	0.6	$18.70^{+1.90}_{-6.20}$
144	26.0	27.0	25.8	76	0.0	1.0	$8.84^{+6.86}_{-0.24}$

Table 2 continued

Table 2 (*continued*)

ID	50% Completeness Limit			Count _{F438W}	dAv	Av	M_{ZAMS}
	F336W	F438W	F814W				
145	26.1	27.1	25.8	32	0.0	2.4	17.27 ^{+1.43} _{-9.97}
146	26.0	26.9	25.5	101	0.0	0.8	21.16 ^{+1.94} _{-8.66}
147	26.1	27.0	26.0	117	0.2	0.8	14.23 ^{+2.87} _{-3.93}
150	26.1	27.1	25.9	143	0.2	2.0	7.53 ^{+5.87} _{-0.23}
152	26.1	26.8	25.6	221	1.2	0.6	20.43 ^{+5.57} _{-7.03}
158	25.9	26.8	25.3	49	0.0	1.2	11.20 ^{+1.30} _{-2.60}
159	26.2	27.2	26.1	86	0.6	1.2	12.06 ^{+5.04} _{-4.36}
165	26.2	27.2	26.1	37	0.0	1.6	8.80 ^{+9.90} _{-1.10}
167	26.0	27.0	25.8	96	0.0	1.4	9.34 ^{+2.36} _{-2.04}
172	26.1	27.1	25.9	135	0.4	1.6	11.43 ^{+3.07} _{-4.13}
174	25.8	26.5	25.2	179	1.6	1.2	20.63 ^{+2.47} _{-12.93}
176	25.9	26.8	25.3	44	0.0	2.4	11.29 ^{+11.81} _{-3.99}
183	26.2	27.2	26.1	113	0.0	0.6	10.59 ^{+1.91} _{-0.29}
184	26.0	26.9	25.5	102	0.0	0.4	24.51 ^{+1.49} _{-14.21}
185	26.1	27.1	25.8	53	0.2	3.0	7.93 ^{+0.17} _{-0.23}
192	26.1	27.0	26.0	108	0.0	0.6	12.41 ^{+10.69} _{-0.71}
194	26.0	26.9	25.6	125	0.0	0.2	10.08 ^{+7.02} _{-0.48}
195	26.0	26.9	25.5	281	0.2	0.4	8.53 ^{+3.17} _{-0.43}
196	26.2	27.2	26.1	108	0.0	0.2	9.95 ^{+2.55} _{-0.35}
197	26.0	26.7	25.1	81	0.0	1.8	7.60 ^{+5.80} _{-0.30}
198	26.2	27.2	26.1	91	0.0	1.2	11.29 ^{+1.21} _{-3.19}
199	26.2	27.2	26.1	161	0.0	2.2	7.93 ^{+10.77} _{-0.63}
201	26.0	27.0	25.8	69	0.0	1.2	8.37 ^{+4.13} _{-0.67}
202	26.3	27.1	26.1	185	0.0	0.2	14.93 ^{+0.77} _{-4.03}
203	26.3	27.0	26.0	232	1.4	1.0	11.45 ^{+7.25} _{-2.85}
204	26.0	27.0	25.9	379	0.0	0.2	15.92 ^{+1.18} _{-5.62}
205	26.2	26.9	26.0	447	2.0	0.2	29.28 ^{+5.42} _{-13.58}
207	25.8	26.8	25.7	242	0.6	0.2	38.64 ^{+3.36} _{-19.94}
208	26.0	27.0	25.8	65	0.0	1.0	14.03 ^{+1.67} _{-5.43}
210	26.2	27.1	26.0	197	0.6	0.6	10.75 ^{+1.75} _{-1.15}
211	26.1	27.0	26.0	176	0.0	0.8	8.99 ^{+3.51} _{-0.39}
213	26.0	26.7	25.1	35	0.0	1.8	10.07 ^{+0.83} _{-2.37}
214	26.3	27.1	26.0	126	0.0	0.2	12.09 ^{+5.01} _{-1.19}
215	26.2	26.9	26.0	161	2.2	0.4	8.03 ^{+10.67} _{-0.33}
216	26.1	27.1	25.9	145	0.0	0.8	8.84 ^{+2.06} _{-0.24}
217	26.0	26.9	25.9	248	0.0	0.2	11.69 ^{+0.81} _{-3.09}

Table 2 continued

Table 2 (*continued*)

ID	50% Completeness Limit			Count _{F438W}	dAv	Av	M_{ZAMS}
	F336W	F438W	F814W				
219	26.2	27.2	26.1	128	0.4	1.0	46.95 ^{+5.15} _{-38.35}
220	26.1	27.1	25.9	139	0.0	0.2	11.21 ^{+0.49} _{-1.61}
224	26.0	26.7	25.1	37	0.0	0.8	7.56 ^{+4.14} _{-0.26}
225	26.5	27.3	26.3	41	0.0	1.0	7.53 ^{+1.47} _{-0.23}
227	26.0	27.1	25.8	46	0.2	0.8	8.35 ^{+6.15} _{-0.25}
228	26.0	27.0	25.8	77	0.0	2.4	7.53 ^{+3.37} _{-0.23}
229	26.0	26.9	25.5	113	0.0	0.6	13.82 ^{+0.68} _{-4.22}
230	26.2	27.2	26.1	102	0.0	1.6	9.33 ^{+3.17} _{-1.63}
231	26.1	27.1	25.8	51	0.0	1.2	8.35 ^{+5.05} _{-0.25}
233	26.3	27.3	26.3	113	0.2	0.4	13.81 ^{+0.69} _{-2.91}
234	26.2	27.2	26.1	131	0.0	0.2	26.60 ^{+2.60} _{-15.70}
235	26.0	26.7	25.1	32	0.0	0.8	11.53 ^{+1.87} _{-2.93}
236	26.0	27.1	25.8	80	0.2	1.8	12.06 ^{+1.34} _{-4.76}
237	26.1	27.1	25.9	100	0.0	0.8	9.38 ^{+5.12} _{-0.38}
238	26.0	27.0	25.9	162	2.0	0.4	8.08 ^{+12.52} _{-0.38}
239	26.3	27.1	26.1	357	1.4	0.6	19.19 ^{+6.81} _{-10.19}
240	25.9	26.9	25.8	210	0.2	0.8	10.74 ^{+3.76} _{-1.14}
241	26.2	27.2	25.9	27	0.2	2.0	9.94 ^{+4.56} _{-2.64}
242	26.0	26.7	25.1	53	0.0	1.8	9.40 ^{+1.50} _{-2.10}
243	26.1	27.1	25.9	945	0.2	0.2	11.54 ^{+4.16} _{-0.64}
245	26.1	27.0	25.9	215	0.0	0.6	10.33 ^{+0.57} _{-1.73}
246	26.2	27.2	26.1	184	0.0	0.2	11.15 ^{+4.55} _{-2.15}
247	26.0	27.1	25.8	357	0.8	0.2	10.60 ^{+2.80} _{-1.00}
248	26.1	27.1	25.8	37	0.0	3.0	10.59 ^{+12.51} _{-3.29}
251	26.2	26.9	26.0	186	0.2	0.6	11.32 ^{+7.38} _{-1.02}
252	26.3	27.1	26.1	201	0.0	0.6	8.67 ^{+3.83} _{-0.57}
253	26.0	26.7	25.1	35	0.0	0.4	11.56 ^{+9.04} _{-1.96}
254	26.2	27.2	26.1	114	0.0	0.4	15.06 ^{+8.04} _{-5.46}
255	26.0	27.1	25.8	183	0.0	0.8	7.58 ^{+9.52} _{-0.28}
256	26.2	27.2	26.1	125	0.0	0.8	8.80 ^{+9.90} _{-0.20}
257	25.9	26.8	25.3	39	0.0	1.0	8.87 ^{+3.63} _{-0.27}
258	26.0	26.8	25.9	400	2.0	0.2	19.02 ^{+1.58} _{-9.42}
259	26.0	26.9	25.9	254	1.8	0.4	36.73 ^{+5.27} _{-25.83}
260	26.1	27.1	25.9	161	1.2	1.8	42.93 ^{+9.17} _{-35.63}
261	25.9	26.9	25.8	162	0.0	1.2	13.13 ^{+1.37} _{-4.53}
262	25.9	26.8	25.3	75	1.0	0.6	7.93 ^{+3.77} _{-0.23}

Table 2 continued

Table 2 (*continued*)

ID	50% Completeness Limit			Count _{F438W}	dAv	Av	M_{ZAMS}
	F336W	F438W	F814W				
263	25.9	26.9	25.8	196	0.0	0.4	10.78 ^{+6.32} _{-0.48}
264	26.0	26.9	25.7	241	0.0	1.0	8.53 ^{+5.97} _{-0.43}
265	26.1	27.0	25.9	227	0.0	1.4	7.54 ^{+3.36} _{-0.24}
266	26.0	27.0	25.8	75	0.2	1.4	9.33 ^{+2.37} _{-2.03}
268	26.0	27.1	25.8	68	0.0	1.6	7.53 ^{+9.57} _{-0.23}
269	25.9	26.9	25.9	236	1.0	0.6	36.24 ^{+5.76} _{-23.74}
270	26.5	27.3	26.3	49	0.8	1.6	10.59 ^{+1.11} _{-2.89}
271	26.0	26.8	25.9	340	2.2	0.4	10.68 ^{+5.02} _{-0.38}
272	26.2	27.2	26.1	127	0.0	1.2	10.63 ^{+3.87} _{-2.53}
273	26.0	27.0	25.8	60	0.0	0.4	9.94 ^{+5.76} _{-0.94}
274	26.0	26.8	25.9	293	1.4	0.4	8.54 ^{+12.06} _{-0.44}
275	26.1	27.1	25.9	228	0.0	0.8	8.96 ^{+2.74} _{-0.36}
276	26.1	27.0	26.0	117	0.6	0.2	59.14 ^{+7.46} _{-45.74}
277	26.1	27.1	25.9	124	0.0	0.6	10.33 ^{+3.07} _{-1.73}
278	26.0	27.0	25.8	60	0.0	1.4	8.80 ^{+4.60} _{-0.20}
279	26.0	26.9	25.7	229	1.0	0.2	19.13 ^{+1.47} _{-7.43}
280	25.9	26.8	25.3	69	0.0	1.2	9.34 ^{+2.36} _{-1.64}
282	26.2	27.2	26.1	99	0.0	0.4	15.07 ^{+0.63} _{-2.57}
283	25.9	26.9	25.8	176	0.2	1.4	10.80 ^{+0.90} _{-1.80}
284	26.1	27.1	25.8	56	0.2	1.8	13.94 ^{+0.56} _{-6.64}
285	26.5	27.3	26.3	33	0.0	2.8	12.95 ^{+53.65} _{-5.65}
286	25.9	26.9	25.8	172	0.0	0.2	7.98 ^{+6.52} _{-0.28}
287	26.1	27.1	25.9	120	0.2	0.8	20.39 ^{+0.21} _{-11.39}
292	26.1	27.0	26.0	111	0.8	0.4	39.88 ^{+2.12} _{-26.48}
293	25.9	26.8	25.3	61	0.0	0.4	24.53 ^{+1.47} _{-14.93}
294	26.0	26.9	25.5	106	0.0	0.4	13.35 ^{+7.25} _{-2.45}
295	26.1	27.1	25.9	105	0.0	0.2	10.68 ^{+3.82} _{-0.38}
296	26.0	26.9	25.5	108	0.0	0.8	9.26 ^{+1.64} _{-0.66}
298	26.2	27.2	26.1	139	0.0	0.2	19.62 ^{+0.98} _{-10.02}
299	25.9	26.9	25.8	156	0.2	0.4	19.04 ^{+1.56} _{-7.34}
302	26.1	27.1	25.9	89	0.2	0.4	30.31 ^{+4.39} _{-16.91}
304	26.1	27.1	25.9	78	0.6	0.6	38.24 ^{+3.76} _{-26.54}
306	26.5	27.3	26.3	48	0.0	1.4	9.33 ^{+9.33} _{-9.33}
SN1923A	26.2	26.9	26.0	234	1.2	0.8	53.31 ^{+13.29} _{-43.71}
SN1950B	26.1	27.1	25.8	39	0.0	3.2	7.56 ^{+3.34} _{-0.26}
SN1957D	26.0	26.9	25.5	78	0.8	0.2	7.56 ^{+8.14} _{-0.26}
SN1983N	25.5	26.4	25.5	293	0.2	0.2	20.43 ^{+5.57} _{-4.73}

Table 3. Age Distribution Results from SNR 295^a

(1)	(2)	(3)	(4)	(5)	(6)	(7)	(8)	(9)	(10)	(11)	(12)	(13)	(14)
T1	T2	SFR (Best)	-err	+err	PDF(Best)	-err	+err	CDF(Best)	CDF(16)	CDF(50)	CDF(84)	M1	M2
4.0	4.5	0.0000e+00	0.0000e+00	6.5843e-04	0.000	0.000	0.075	0.000	0.000	0.000	0.033	52.1	66.6
4.5	5.0	0.0000e+00	0.0000e+00	5.7722e-04	0.000	0.000	0.074	0.000	0.000	0.018	0.057	42.0	52.1
5.0	5.6	0.0000e+00	0.0000e+00	6.3443e-04	0.000	0.000	0.089	0.000	0.002	0.034	0.083	34.7	42.0
5.6	6.3	0.0000e+00	0.0000e+00	5.4562e-04	0.000	0.000	0.087	0.000	0.012	0.049	0.108	29.2	34.7
6.3	7.1	0.0000e+00	0.0000e+00	5.1369e-04	0.000	0.000	0.091	0.000	0.023	0.065	0.133	26.0	29.2
7.1	7.9	0.0000e+00	0.0000e+00	4.3090e-04	0.000	0.000	0.086	0.000	0.033	0.080	0.156	23.1	26.0
7.9	8.9	0.0000e+00	0.0000e+00	4.4905e-04	0.000	0.000	0.099	0.000	0.044	0.097	0.182	20.6	23.1
8.9	10.0	0.0000e+00	0.0000e+00	4.8762e-04	0.000	0.000	0.118	0.000	0.057	0.117	0.213	18.7	20.6
10.0	11.2	1.5681e-03	1.1463e-03	2.4191e-04	0.242	0.192	0.249	0.242	0.155	0.265	0.412	17.1	18.7
11.2	12.6	0.0000e+00	0.0000e+00	3.6069e-04	0.000	0.000	0.111	0.242	0.172	0.284	0.440	15.7	17.1
12.6	14.1	0.0000e+00	0.0000e+00	3.7103e-04	0.000	0.000	0.126	0.242	0.190	0.305	0.473	14.5	15.7
14.1	15.8	0.0000e+00	0.0000e+00	3.5337e-04	0.000	0.000	0.134	0.242	0.210	0.327	0.507	13.4	14.5
15.8	17.8	0.0000e+00	0.0000e+00	3.5393e-04	0.000	0.000	0.148	0.242	0.230	0.351	0.544	12.5	13.4
17.8	20.0	0.0000e+00	0.0000e+00	3.8747e-04	0.000	0.000	0.175	0.242	0.254	0.380	0.585	11.7	12.5
20.0	22.4	3.2132e-35	3.2132e-35	3.5257e-04	0.000	0.000	0.179	0.242	0.279	0.409	0.629	10.9	11.7
22.4	25.1	1.9962e-03	1.3454e-03	4.9830e-05	0.688	0.469	0.165	0.930	0.579	0.755	0.892	10.3	10.9
25.1	28.2	0.0000e+00	0.0000e+00	2.7900e-04	0.000	0.000	0.178	0.930	0.616	0.788	0.919	9.6	10.3
28.2	31.6	1.6137e-04	1.6137e-04	6.6697e-04	0.070	0.070	0.383	1.000	0.741	0.874	0.978	9.0	9.6
31.6	35.5	0.0000e+00	0.0000e+00	2.8913e-04	0.000	0.000	0.220	1.000	0.793	0.913	1.000	8.6	9.0
35.5	39.8	0.0000e+00	0.0000e+00	2.4359e-04	0.000	0.000	0.211	1.000	0.846	0.955	1.000	8.1	8.6
39.8	44.7	0.0000e+00	0.0000e+00	2.2500e-04	0.000	0.000	0.217	1.000	0.909	1.000	1.000	7.7	8.1
44.7	50.1	0.0000e+00	0.0000e+00	2.0419e-04	0.000	0.000	0.220	1.000	1.000	1.000	1.000	7.3	7.7

^a Similar tables are available for all fitted SNRs with inferred progenitor masses in the supplemental materials.

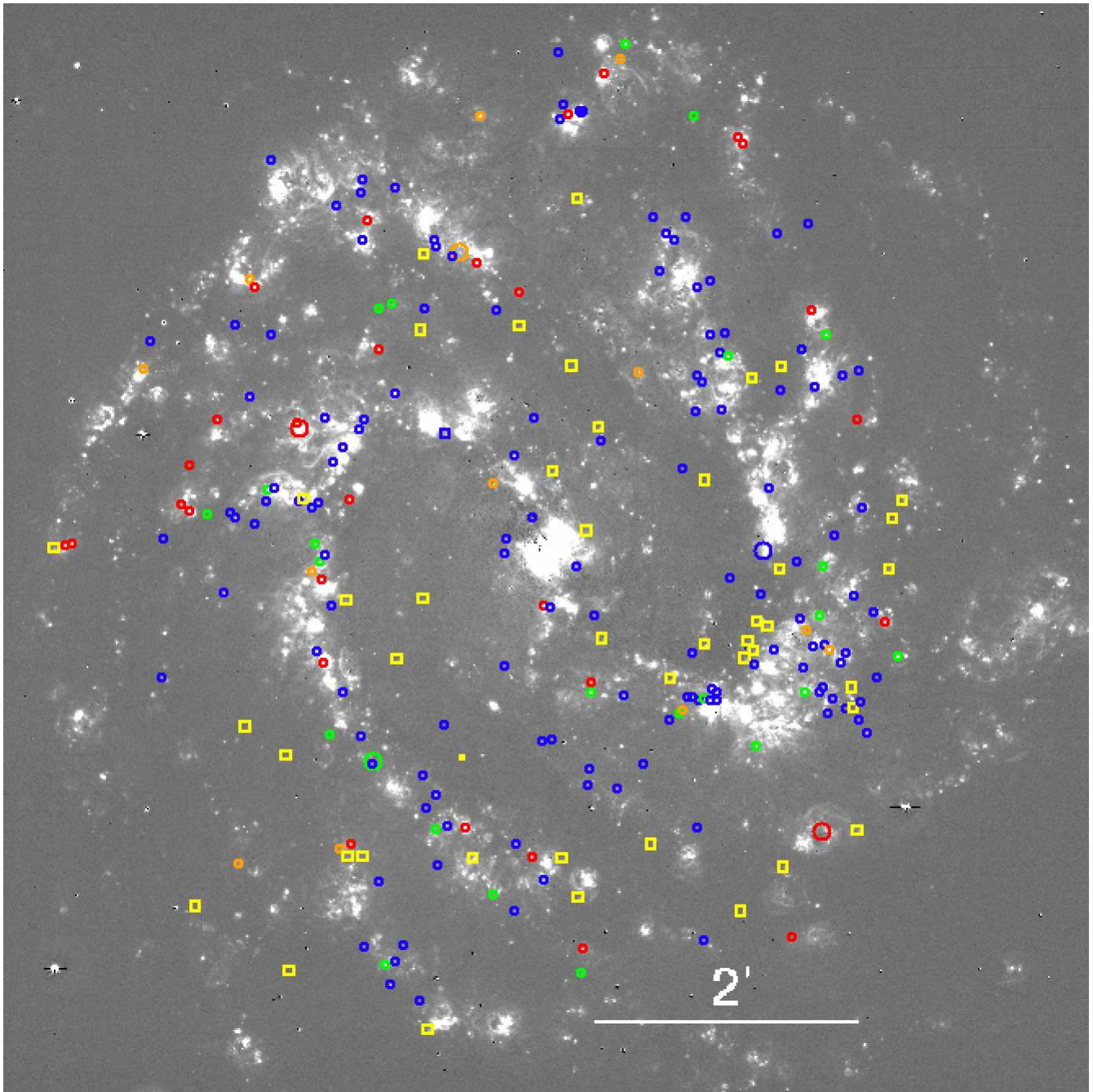


Figure 1. Locations of M83 SNRs color-coded by the progenitor masses inferred from their local stellar populations are overlotted on a continuum-subtracted $H\alpha$ image from the Magellan telescope (Blair et al. 2012). Colored circles indicate: red = $>20 M_{\odot}$; orange = $16-20 M_{\odot}$; green = $12-16 M_{\odot}$; blue = $<12 M_{\odot}$. SNRs with no local young population (Type Ia candidates) are plotted as open yellow squares. Slightly larger circles show positions of historical SNe for which we derived progenitor masses.

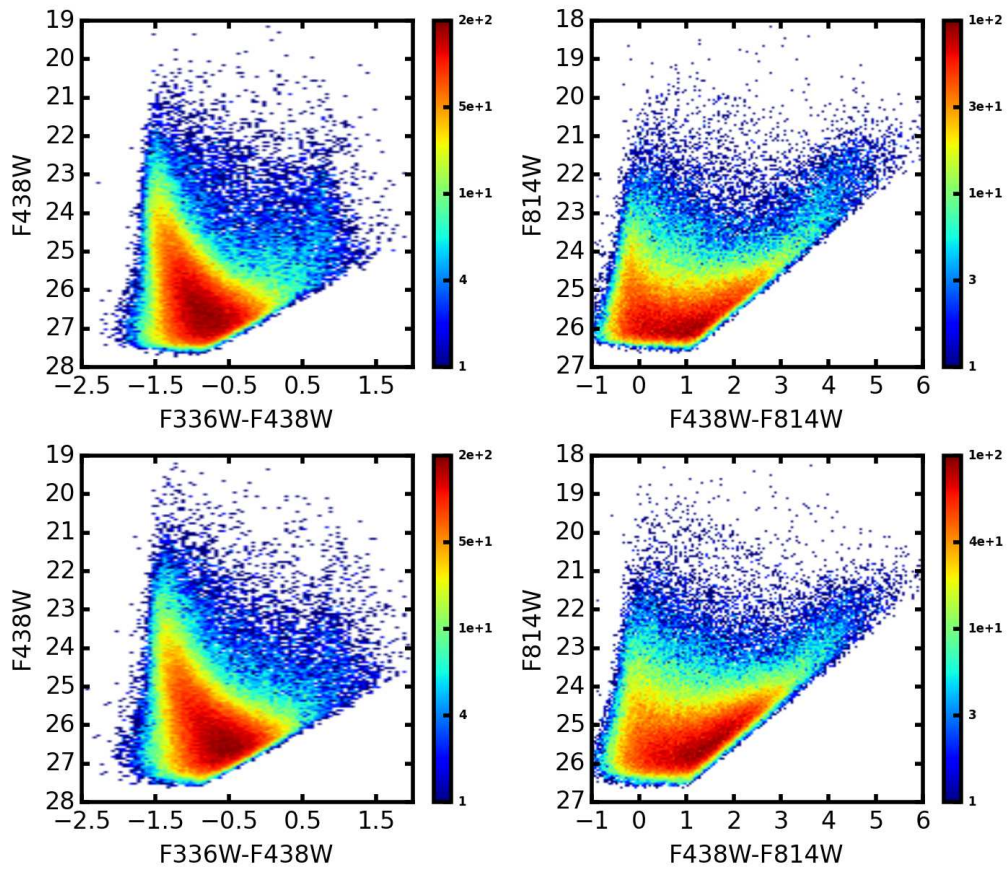


Figure 2. Color-magnitude diagrams for the three UV/Optical bands for two fields of the seven field mosaic of M83. These are (*upper-left*) UV CMD for The POS2 field, (*upper-right*;) optical CMD for the POS2 field, (*lower-left*;) UV CMD for the F5 field, and (*lower-right*;) optical CMD for the F5 field.

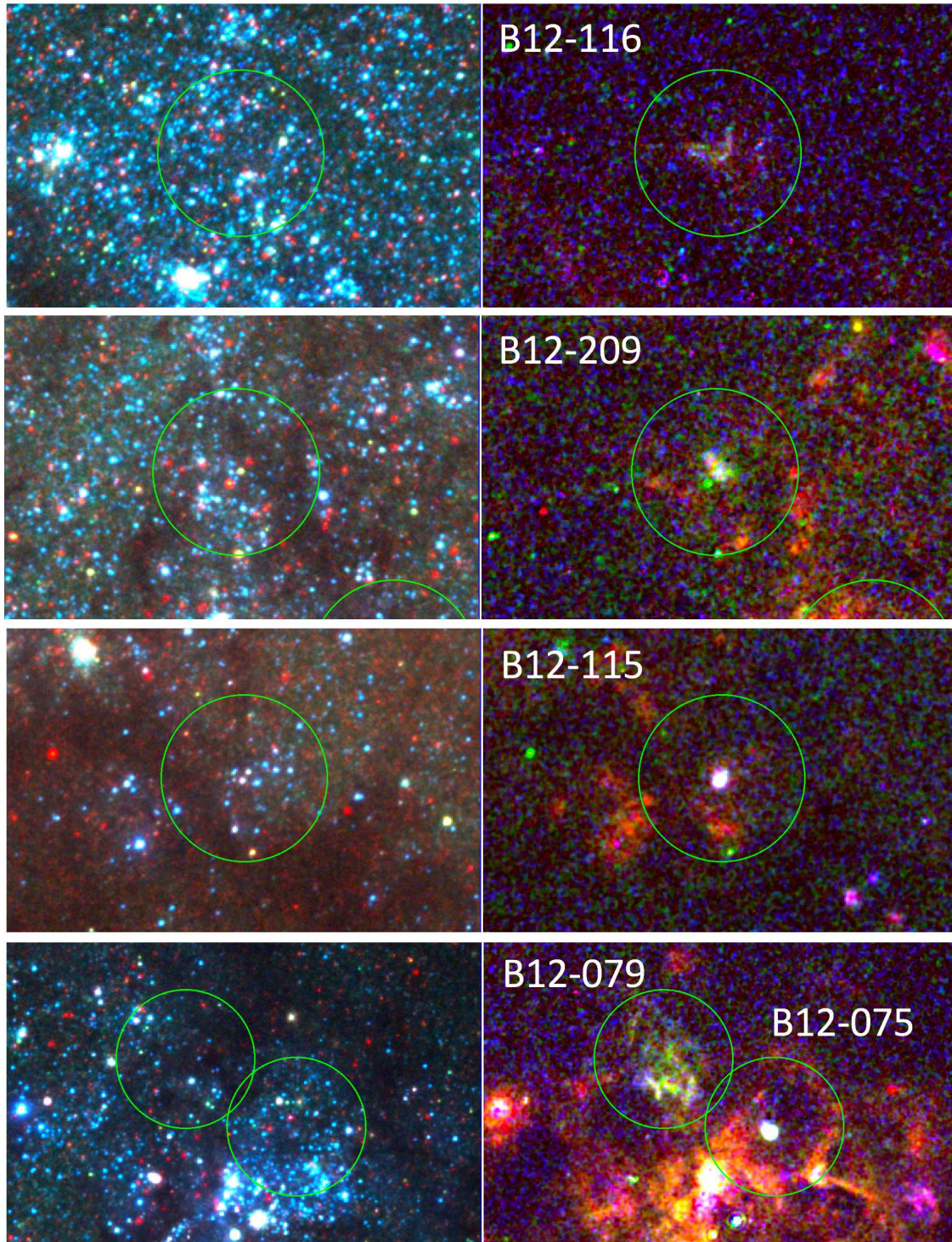


Figure 3. Example fields showing the range of star colors, star density, and impacts from dust absorption encountered in the 100 pc fitting regions around several M83 SNRs. All data shown are from HST WFC3 imaging and the green circles are 100 pc in diameter at the assumed distance of M83. Each two-panel pairing shows a three-color image of stellar data on the left (red = F814W, green = F438W, blue = F336W), and a three color continuum-subtracted emission line image on the right (red = H α , green = [S II], blue = [O III]). Identifications for the SNRs are from Blair et al. (2012) and are shown on the emission line panels.

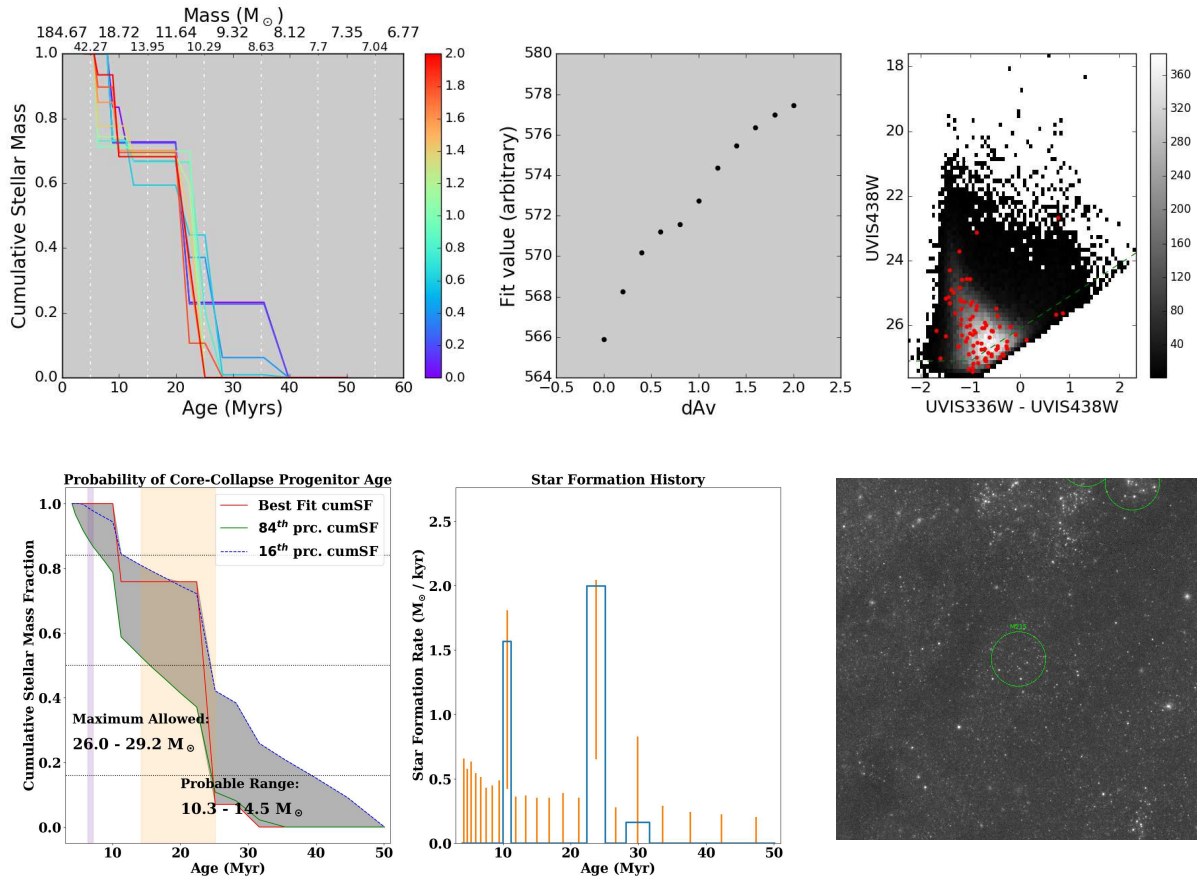


Figure 4. Technique for constraining SNR progenitor mass (SNR 295). *Bottom right:* The extraction region for the resolved stellar photometry sample is shown as a green circle on a $20'' \times 20''$ F438W image of the region of interest for this SNR. *Top right:* The observed CMD from the extraction photometry. The photometry of the stars in the surrounding field are shown in grayscale, where the lighter colors mark regions of the CMD that have more field stars, as indicated by the color bar. The photometry of the stars within 50 pc of the SNR location are overplotted in red points. The magnitude limits of the data included in the CMD fitting are shown by the dashed lines. These limits are based on the completeness for regions with the stellar density of this location as determined by the ASTs (see § 2.3). *Top left:* Multiple SFH measurements, assuming different amounts of differential reddening (dA_V) at the SNR location. Lines show the cumulative fraction of stellar mass in each age interval. Various colors denote the amount of dA_V , as indicated by the color bar. *Top center:* Maximum likelihood fit values as a function of assumed dA_V . Lower values indicate a better fit to the data. In this example, we adopt a dA_V value of zero for the final fitting, as this value produces the best fit. *Bottom left:* The cumulative fraction of stellar mass in each age interval for the final SFH fit, along with uncertainties from the HybridMC error analysis. The probable mass range listed is the range of ages consistent (1σ uncertainty) with the population median age, marked with the tan shading. The maximum allowed progenitor mass is the most massive star allowed in this location by the uncertainties in the youngest age bins. *Bottom center:* The differential SFH, showing the star formation rates and uncertainties that correspond to the cumulative fraction plot in *bottom left*. Note that bins with large uncertainties have a large covariance with neighboring bins, which makes the cumulative distribution easier to interpret. We include figures of this format for all 199 SNRs with progenitor constraints in the supplemental materials.

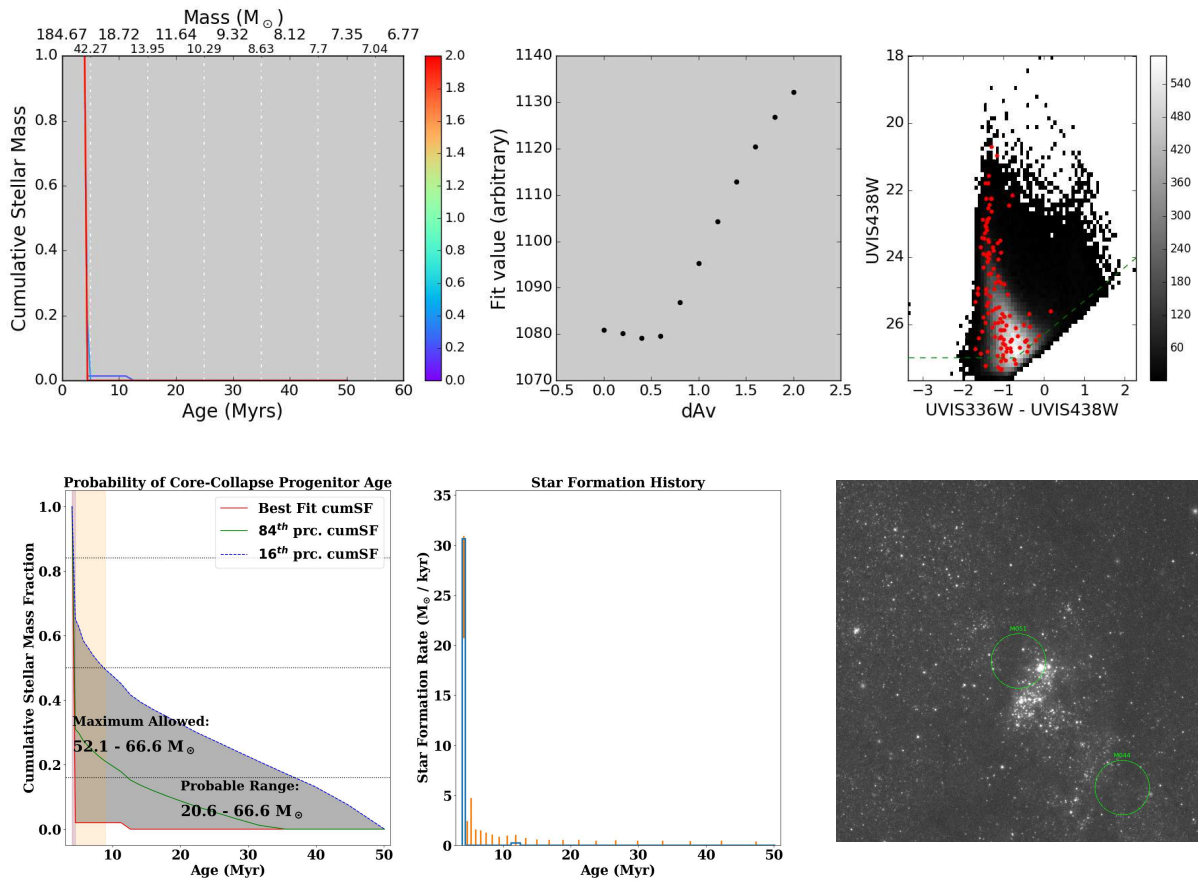


Figure 5. Same as Figure 4, but for 057. We provide this second example to show an extreme case, as 057 has the youngest age constraint of the entire sample.

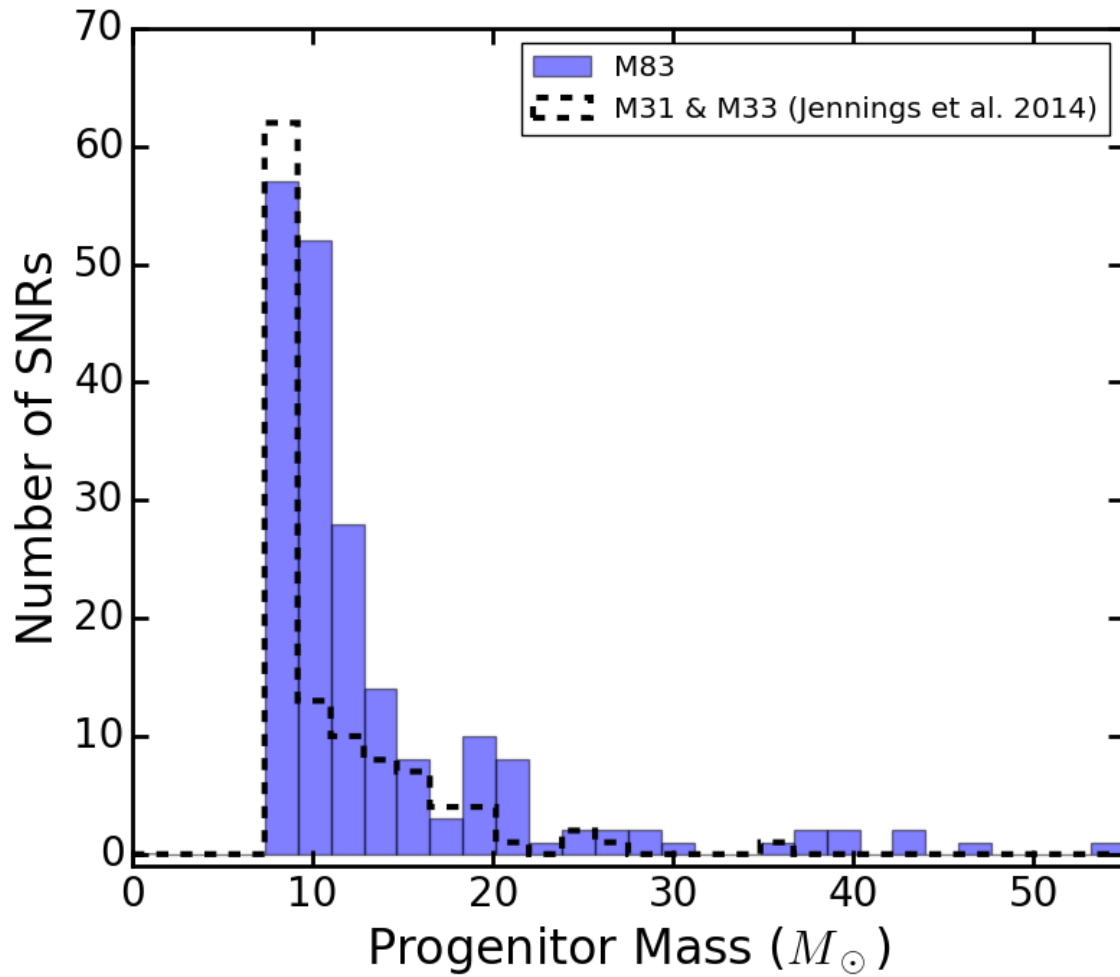


Figure 6. The M83 distribution of progenitor masses is shown by the blue histogram, with the M31+M33 distribution (dashed line) for comparison. The M83 sample has many more SNRs with measurements at masses $>10 M_{\odot}$ but is not as dominated by the lowest mass bin. M83 also has a significant tail to higher masses, with a number of bona fide progenitor masses in excess of $30 M_{\odot}$. The cutoff at lower masses was actually measured for the M31+M33 sample (Díaz-Rodríguez et al. 2018), but was assumed for this work on M83 (see Section 2.7 for details).

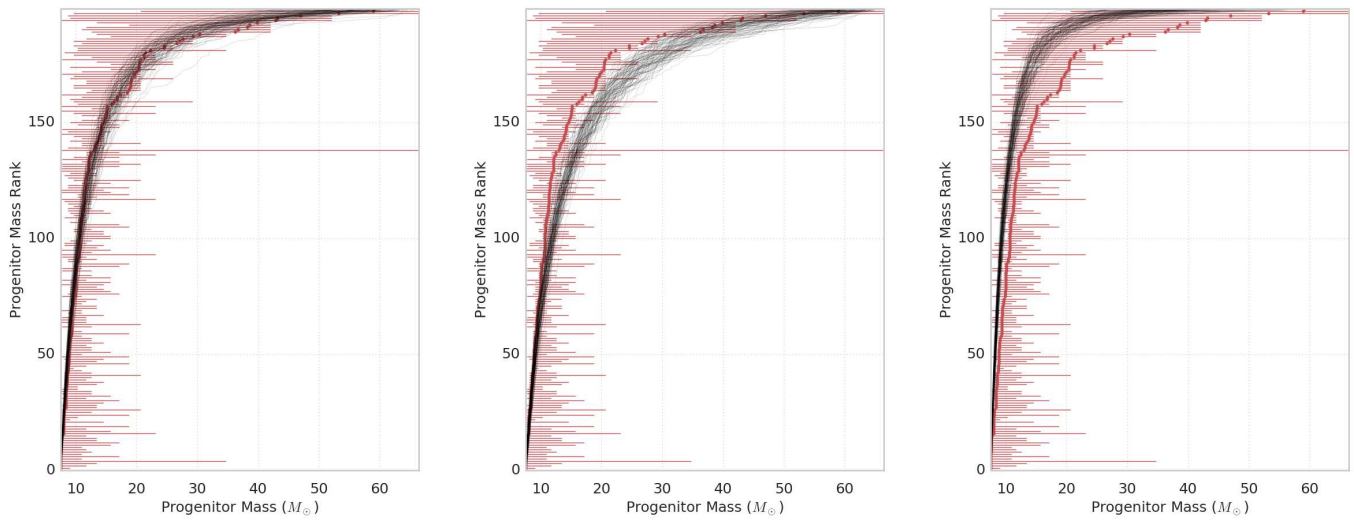


Figure 7. The ranked distribution of progenitor masses for the 199 measurements we obtained from from the M83 sample are plotted with red horizontal error bars. Overplotted with gray lines in each panel are 50 draws from a power-law distribution. While all 3 panels show the same progenitor masses in red, the power-law plotted in gray is different for each panel as follows: *Left:* The best-fitting power law index of $-2.9^{+0.2}_{-0.7}$; *Middle* A Salpeter index (-2.35); *Right:* The best-fit index from the combined M31/M33 SNR progenitor sample measurements from (-4.4; J14).